Elys deficiency constrains Kras-driven tumour burden by amplifying oncogenic stress

Kimberly J Morgan[1,2], Karen Doggett[1,2], Fan-Suo Geng[1,3], Lachlan Whitehead[2,4], Kelly A Smith[5,6], Benjamin M Hogan[6,7], Cas Simons[6,8], Gregory J Baillie[6], Ramyar Molania[2,9], Anthony T Papenfuss[2,9], Thomas E Hall[6], Elke A Ober[10], Didier Y R Stainier[11], Zhiyuan Gong[12] and Joan K Heath[1,2,*]

[1]Epigenetics and Development Division, Walter and Eliza Hall Institute of Medical Research, Parkville, Victoria 3052, Australia

[2]Department of Medical Biology, University of Melbourne, Parkville, Victoria 3010, Australia

[3]Genomics and Epigenetics Division, Garvan Institute of Medical Research, Darlinghurst, New South Wales, Australia and St Vincent's Clinical School, Faculty of Medicine, University of New South Wales, New South Wales 2010, Australia

[4]Centre for Dynamic Imaging, Advanced Technology and Biology Division, Walter and Eliza Hall Institute of Medical Research, Parkville, Victoria 3052, Australia

[5]Department of Physiology, The University of Melbourne, Parkville, Victoria 3010, Australia

[6]Institute for Molecular Biosciences, The University of Queensland, Brisbane, Queensland 4072, Australia

[7]Peter MacCallum Cancer Centre, Melbourne, Victoria 3000, Australia

[8]Murdoch Children's Research Institute, Parkville, Victoria 3052, Australia

[9]Bioinformatics Division, Walter and Eliza Hall Institute of Medical Research, Parkville, Victoria 3052, Australia

23 [10]Danish Stem Cell Center, University of Copenhagen, 2200 Copenhagen N, Denmark

24 [11]Max Planck Institute for Heart and Lung Research, Dept. III – Developmental Genetics

25 Ludwigstrasse 43, 61231 Bad Nauheim, Germany

26 [12]Department of Biological Science, National University of Singapore, Singapore

27 ***Corresponding Author:** Joan K Heath, Walter and Eliza Hall Institute of Medical Research, 1G Royal

28 Parade, Parkville, Victoria 3052, Australia. Phone: (+613) 9345-2872

29 Email: joan.heath@wehi.edu.au

30 **Declaration of interests**: The authors declare no potential conflicts of interest

31

ABSTRACT

The nucleoporin ELYS, encoded by *AHCTF1*, is a large multifunctional protein with essential roles in nuclear pore assembly and mitosis. Using a zebrafish model of hepatocellular carcinoma, in which the expression of an inducible mutant *kras* transgene *(kras^{G12V})* drives hepatocyte-specific hyperplasia and liver enlargement, we show that reducing *ahctf1* gene dosage by 50% markedly shrinks tumour burden, while non-hyperplastic tissues are unaffected. We demonstrate that *ahctf1* heterozygosity impairs nuclear pore formation, mitotic spindle assembly and chromosome segregation, leading to DNA damage and activation of TP53-dependent and independent mechanisms of cell death and cell cycle arrest. This selective vulnerability of cancer cells to mild disruption of Elys function uncovers a novel synthetic lethal interaction between *ahctf1* and oncogenic *kras* that could be exploited therapeutically. Heterozygous expression of both *ahctf1* and *ranbp2*, or treatment of heterozygous *ahctf1* larvae with the nucleocytoplasmic transport inhibitor, Selinexor, completely blocked *kras^{G12V}*-driven hepatocyte hyperplasia, revealing promising avenues for combinatorial treatments.

46 **INTRODUCTION**

47 Synthetic lethality is the term used to describe the death of cells in response to co-existing
48 disruptions in two different genes, neither of which is lethal alone. The phenomenon has emerged
49 as a promising tool for cancer drug development[1]. The advantage of the approach lies in its capacity
50 to induce the death of a vulnerable cell population, such as oncogene-expressing cancer cells, while
51 healthy cells are unaffected. The approach has been validated in the clinic by the use of
52 poly(adenosine diphosphate [ADP]-ribose) polymerase (PARP) inhibitors to treat tumours carrying
53 mutations in the breast cancer susceptibility genes, *BRCA1*/*BRAC2*[2], and its success has fuelled the
54 search for other clinically relevant pairwise combinations. Particular effort has been directed
55 towards identifying genes whose partial loss of function confers synthetic lethality in cancer cells
56 containing hitherto 'undruggable' oncogene targets, such as mutant *KRAS*[3,4]. In this paradigm, the
57 interacting gene is not mutated in cancer nor oncogenic in its own right; however, its function is
58 essential to maintain the tumourigenic state, inspiring the concept of non-oncogene addiction[5].

59 In this paper, we tested whether *AHCTF1* exhibits the properties of a mutant *KRAS* synthetic lethal
60 interacting gene. *AHCTF1* encodes ELYS, a 252 kDa multidomain nucleoporin that was first
61 discovered in mouse development where it was shown to be required for the proliferation and
62 survival of inner mass cells[6]. Since then, ELYS has been studied in many model systems, including in a
63 zebrafish development mutant (ti262)[7], where we and others showed that homozygous inheritance
64 of an ENU-induced nonsense mutation in *ahctf1* disrupted nuclear pore formation and caused
65 catastrophic levels of cell death in highly proliferative cell compartments, such as the intestinal
66 epithelium, while relatively quiescent tissues survived and remained healthy[8,9].

67 That ELYS is selectively required by proliferating cells is not unexpected given the multiple roles it
68 plays in the cell cycle (Fig. 1). As well as being a structural component of nuclear pore complexes
69 (NPCs), ELYS is essential for their formation at the end of mitosis[10-12]. NPCs are huge (110 MDa)
70 multi-subunit complexes comprising at least 30 different nucleoporins (Nups) in an octameric

71 array[13]. They form cylindrical channels in the nuclear envelope (NE) and regulate nucleocytoplasmic
72 transport and intracellular localisation of large (>40 kDa) molecules. In the absence of ELYS, the NE is
73 re-built at the end of mitosis but this occurs without NPC formation, precluding mRNAs and large
74 proteins from moving in and out of the nucleus. By providing a platform for NPC re-assembly at the
75 end of mitosis (Fig. 1a,b), ELYS restores nucleocytoplasmic trafficking, and thereby facilitates entry
76 into the nucleus of proteins such as G1 and S phase cyclin-dependent kinases that are required for
77 DNA replication and cell cycle progression (Fig. 1c). Also in G1/S phase, ELYS regulates transcription
78 and DNA replication by reversible binding to components of the SWI/SNF 80 chromatin remodeller
79 complex, PBAP, and the DNA replication origin licensing system, MCM2-7, respectively (Fig. 1d-
80 f)[11,12,14,15].

81 At the end of G2, the cell has grown to a critical size and is prepared for M phase (Fig. 1g). The NE
82 breaks down (NEBD) and NPCs are disassembled (Fig. 1h). Whereas most Nups disperse throughout
83 the cytoplasm and the endoplasmic reticulum (ER)[16,17], ELYS, together with components of the
84 Nup107-160 complex and RANBP2, play an important role in prophase by binding to the
85 kinetochores of recently replicated sister chromatids where they contribute to microtubule
86 recruitment and spindle assembly (Fig. 1i)[18-20]. At telophase, when the chromatids are fully
87 separated, the spindle and kinetochores dissolve and ELYS becomes tethered to thousands of sites
88 on chromatin through its C-terminal chromatin binding region where it promotes chromatin
89 decondensation[15,21]. In G1, the N-terminal half of ELYS provides a scaffold to bind the Nup107-160
90 complex and other ER-associated Nups, thereby coupling the initiation of NPC assembly with
91 euchromatin formation, restoration of nucleocytoplasmic transport and transcription[11,22,23].

92 Given this plethora of functions throughout the cell cycle, it is not surprising that ELYS is an Achilles'
93 heel of highly proliferative cells[8,9]. To test whether this vulnerability extrapolates to cancer cells *in*
94 *vivo*, we employed a highly tractable zebrafish model of hepatocellular carcinoma (HCC) in which
95 hepatocyte hyperplasia and liver enlargement are driven by an inducible, hepatocyte-specific *EGFP-*
96 *kras*^{G12V} transgene[24]. In this study, we used two-photon microscopy to accurately quantitate liver

97 volume in the presence and absence of a single nonsense mutation in one allele of the *ahctf1*
98 locus[8,9]. Remarkably, we observed a pronounced reduction in tumour burden in response to this
99 mild (50%) reduction in *ahctf1* gene dosage, while the rest of the animal was unaffected. We further
100 show that this selective vulnerability of oncogenic *kras*^{G12V}-expressing liver cancer cells to *ahctf1*
101 heterozygosity possesses the hallmarks of a synthetic lethal interaction that may be exploited
102 therapeutically.

103

104 **RESULTS**

105 ***ahctf1* heterozygosity reduces tumour burden in a zebrafish *kras^{G12V}*-driven model of**
106 **hepatocellular carcinoma**

107 In the zebrafish *kras^{G12V}*-driven HCC model, the doxycycline-induced expression of a single *EGFP-*
108 *kras^{G12V}* transgene (genotype denoted *TO(kras^{G12V})$^{T/+}$* between 2-7 days post-fertilisation (dpf) leads
109 to the accumulation of a constitutively active, EGFP-tagged oncogenic form of Kras specifically in
110 hepatocytes[24] (Fig. 2a). This forced expression of *EGFP-kras^{G12V}* causes hepatocyte hyperplasia and a
111 substantial increase in liver volume that can be quantified by two-photon microscopy. To investigate
112 the role of Elys in a cancer setting, we introduced a mutant *ahctf1* allele (containing a nonsense
113 mutation at codon 1319) from a zebrafish development mutant (*flo*^{ti262})[7] into the genome of this
114 model. This resulted in a 57% reduction in *ahctf1* mRNA expression in *ahctf1$^{+/-}$* larvae at 7 dpf (Fig.
115 2b), indicating that the premature codon encoded by the nonsense mutation triggers nonsense
116 mediated decay rather than expression of a truncated Elys protein.

117 To determine the effect of *ahctf1* heterozygosity (and other treatments) on normal liver cells, we
118 used a control transgenic line, denoted *2-CLiP* (2-Colour Liver Pancreas), in which hepatocytes
119 express dsRed fluorescence but no oncogenic transgene[25]. We found that the mean liver volume in 7
120 dpf wildtype zebrafish larvae is 1.95 x 10^6 ± 4.99 x 10^4 μm^3 (Fig. 2c,d). *ahctf1* heterozygosity had no
121 significant impact on liver volume in this model, consistent with previous observations that *ahctf1*
122 heterozygotes develop normally, reach sexual maturity, and exhibit a normal lifespan[9].

123 Turning to the *TO(kras^{G12V})* model, we found that induced expression of oncogenic Kras^{G12V} led to
124 liver hyperplasia and a striking (4.1-fold) increase in liver volume to 7.97 x 10^6 ± 1.21 x 10^5 μm^3. This
125 amounted to an increment in liver volume of approximately 6.02 x 10^6 μm^3 over the course of 5 d,
126 demonstrating the potency of the oncogenic *kras^{G12V}* signal. Remarkably, the excess liver volume
127 was reduced by 35% in livers of *ahctf1$^{+/-}$;TO(kras^{G12V})$^{T/+}$* larvae (down to 5.92 x 10^6 ± 8.83 x 10^4 μm^3).
128 These data demonstrate that a mild (50%) reduction in *ahctf1* gene dosage is sufficient to restrict

129 tumour burden in livers expressing oncogenic *kras*^{G12V}, while having no effect on normal livers. These
130 results demonstrate that reduced *ahctf1* expression is a selective vulnerability of cancer cells and
131 identify a novel synthetic lethal interaction between *ahctf1* and *kras*^{G12V}.

132 Robust and persistent overexpression of RAS oncoproteins is frequently associated with oncogene-
133 induced stress comprising defects in DNA replication, DNA damage and genome instability. In the
134 presence of wildtype TP53, this damage is limited by activation of TP53 transcription pathways that
135 induce cell cycle arrest, senescence and apoptosis. To determine whether expression of *kras*^{G12V}
136 causes oncogene-induced stress and Tp53 activation in our model, we measured the levels of Tp53
137 protein in pooled lysates of micro-dissected *TO(kras*^{G12V}*)*$^{+/+}$ and *TO(kras*^{G12V}*)*$^{T/+}$ livers and the remains
138 of the larvae (Fig. 2e,f). No Tp53 signal was obtained from non-*kras*^{G12V}-expressing livers or the body
139 remains after liver removal. We detected a weak Tp53 signal in extracts of *ahctf1*$^{+/+}$*;TO(kras*^{G12V}*)*$^{T/+}$
140 livers, indicating that expression of the *kras*^{G12V} oncogene alone elicited a weak Tp53 response. In
141 contrast, a much stronger Tp53 signal (>3.5-fold) was detected in *ahctf1*$^{+/-}$*;TO(kras*^{G12V}*)*$^{T/+}$ livers,
142 demonstrating a more severe level of stress in *ahctf1*$^{+/-}$ hepatocytes expressing oncogenic *kras*^{G12V}
143 than occurs in *ahctf1*$^{+/+}$ hepatocytes.

144 **Loss of Tp53 function enhances *kras*^{G12V}-driven liver enlargement, which is partially alleviated by**
145 ***ahctf1* heterozygosity**

146 To test whether activation of the Tp53 pathway was involved in reducing the volume of *kras*^{G12V}-
147 expressing livers on a heterozygous *ahctf1* background, we repeated the experiment in the absence
148 of Tp53 function. Here, we utilised the zebrafish *tp53*^{e7} or *tp53*^{M214K} allele, which affects a conserved
149 amino acid residue within a region of the Tp53 DNA-binding domain corresponding to a mutational
150 hotspot in human cancer, producing a transactivation-dead Tp53 variant[26]. Abrogating Tp53 function
151 by homozygous expression of this allele (which we denoted *tp53*$^{m/m}$) in *ahctf1*$^{+/+}$*;TO(kras*^{G12V}*)*$^{T/+}$
152 larvae supported a further large increase (82%) in excess liver volume ($1.25 \times 10^7 \pm 1.10 \times 10^5$ μm^3)
153 compared to livers on the *tp53*$^{+/+}$ background (Fig. 2g,h) (Supplementary Fig. 1-3). These data

154 indicate that Tp53 function normally restrains tumour growth and liver enlargement in this model.
155 Nonetheless, the excess liver volume ($9.82 \times 10^6 \pm 1.34 \times 10^5$ μm^3) on the *ahctf1*$^{+/-}$
156 ;*tp53*$^{m/m}$;*TO(kras*^{G12V}*)*$^{T/+}$ background was 35% less than on a wildtype *ahctf1* background, indicating
157 that mildly disrupted *ahctf1* expression can reduce tumour burden, even in the complete absence of
158 functional Tp53.

159 ***ahctf1* heterozygosity triggers cell death in *TO(kras*^{G12V}*)*$^{T/+}$ hepatocytes that is partially Tp53-**
160 **independent**

161 As expression of Tp53 was upregulated in *ahctf1*$^{+/-}$;*TO(kras*^{G12V}*)*$^{T/+}$ livers, we next determined
162 whether the reduction in liver volume in heterozygous *ahctf1* larvae was due to the induction of a
163 Tp53-dependent cell death response. To investigate this, we utilised a transgenic line, Tg(*actb2:SEC-*
164 *Hsa.ANXA5-mKate2,cryaa:mCherry*)^{uq24rp} (hereafter denoted *Annexin 5-mKate*) that constitutively
165 expresses a fusion protein comprising Annexin 5 and the far-red fluorophore mKate[27]. This fusion
166 protein identifies cells undergoing apoptosis by binding to phosphatidylserine that is normally
167 inaccessible on the inner leaflet of the plasma membrane but is exposed as the membrane breaks
168 down. This gives rise to discrete fluorescent puncta, which we captured using confocal imaging.

169 Annexin 5 fluorescent puncta were sparsely distributed (1.5 puncta per 10^{-5} μm^3) throughout the
170 livers of *ahctf1*$^{+/+}$;*tp53*$^{+/+}$;*TO(kras*^{G12V}*)*$^{T/+}$ larvae demonstrating that expression of *kras*^{G12V} is
171 associated with low levels of cell death (Fig. 3a,b). In marked contrast, the number of Annexin 5
172 fluorescent objects was 3.5-fold higher (5.2 puncta per 10^{-5} μm^3) in the livers of *ahctf1*$^{+/-}$
173 ;*tp53*$^{+/+}$;*TO(kras*^{G12V}*)*$^{T/+}$ larvae demonstrating that the reduction in tumour burden observed in
174 response to *ahctf1* heterozygosity is due, at least in part, to an increase in cell death (Fig. 3a,b left
175 two columns). These results were recapitulated when the cleaved, (active form) of caspase 3 was
176 used as an alternative marker of apoptosis (Supplementary Fig. 4). That cell death in hyperplastic
177 hepatocytes is largely dependent on Tp53 function was demonstrated by negligible apoptosis in the
178 livers of *ahctf1*$^{+/+}$;*tp53*$^{m/m}$;*TO(kras*^{G12V}*)*$^{T/+}$ larvae (Fig. 3a,b right two columns). Again, the effect of

179 Tp53 loss was partially alleviated by *ahctf1* heterozygosity. We observed a 17.6-fold increase in the
180 abundance of Annexin 5 fluorescent puncta in *tp53*$^{m/m}$*;TO(kras*^{G12V}*)*$^{T/+}$ livers on a heterozygous
181 *ahctf1*$^{+/-}$background, compared to livers on a *ahctf1*$^{+/+}$ background.

182 We showed that the elevated level of Tp53 protein observed in *ahctf1*$^{+/-}$*;TO(kras*^{G12V}*)*$^{T/+}$ livers,
183 compared to *ahctf1*$^{+/+}$*;TO(kras*^{G12V}*)*$^{T/+}$ livers (Fig. 2e,f), was transcriptionally active by the upregulated
184 (4.7-fold) mRNA expression of a canonical Tp53 target gene, *mdm2* (Fig. 3c). This prompted us to
185 quantify the mRNA expression levels of a suite of Bcl2 family genes that regulate intrinsic
186 (mitochondrial) apoptosis (Fig. 3c). Direct Tp53 transcriptional targets, *pmaip1* (aka *noxa*) and *bbc3*
187 (aka *puma*), were both upregulated by >6.5-fold in *ahctf1*$^{+/-}$*;tp53*$^{+/+}$*;TO(kras*^{G12V}*)*$^{T/+}$ livers compared to
188 *ahctf1*$^{+/+}$*;tp53*$^{+/+}$*;TO(kras*^{G12V}*)*$^{T/+}$ livers. mRNAs encoding the other BH3-only apoptosis effector
189 proteins, Bim, Bid, Bik and Bad, and the pro-apoptotic executioner protein, Bax were also increased
190 in *ahctf1*$^{+/-}$*;tp53*$^{+/+}$*;TO(kras*^{G12V}*)*$^{T/+}$ livers compared to *ahctf1*$^{+/+}$*;tp53*$^{+/+}$*;TO(kras*^{G12V}*)*$^{T/+}$ livers.
191 Meanwhile, transcripts encoding Bcl2 and Bclxl pro-survival proteins were significantly
192 downregulated by *ahctf1* heterozygosity. In the absence of Tp53 function, *ahctf1* heterozygosity still
193 increased the expression of these pro-apoptotic transcripts, albeit less markedly. All these data are
194 consistent with induction of Tp53 target genes playing a major role in the cell death response to
195 *ahctf1* heterozygosity in *kras*^{G12V}-expressing livers. Notwithstanding this, *ahctf1* heterozygosity still
196 promotes moderate levels of cell death concomitant with reduced tumour burden, even in the
197 complete absence of Tp53 function.

198 **_ahctf1_ heterozygosity restricts DNA replication in _TO(kras_^{G12V}_)_$^{T/+}$ hepatocytes**

199 To explore whether the reduction in liver enlargement we observe in *ahctf1*$^{+/-}$*;TO(kras*^{G12V}*)*$^{T/+}$ larvae
200 also involves impaired cell cycle progression, we used an EdU incorporation assay to identify cells in
201 S phase (Fig. 4a). We observed 32% EdU-positive cells in the enlarged livers of
202 *ahctf1*$^{+/+}$*;tp53*$^{+/+}$*;TO(kras*^{G12V}*)*$^{T/+}$ larvae and >20% EdU-positive cells (32% reduction) in the livers of
203 *ahctf1*$^{+/-}$*; tp53*$^{+/+}$*;TO(kras*^{G12V}*)*$^{T/+}$ larvae (Fig. 4b,c). In Tp53 deficient larvae, liver volume was markedly

204 increased as expected (Fig. 4b) and there was a doubling in the percentage of EdU-positive cells
205 (63% compared to 32%) (Fig. 4c). *ahctf1* heterozygosity reduced liver volume in both Tp53 proficient
206 and deficient larvae (Fig. 4b), consistent with Fig. 2, and reduced the percentage of EdU-positive
207 cells in both Tp53 proficient (22% compared to 32%) and Tp53 deficient larvae (53% compared to
208 63%) (Fig. 4c). These data indicate that the overall reduction in liver tumour burden we observe in
209 response to *ahctf1* heterozygosity is due to reduced numbers of cycling cells and increased numbers
210 of apoptotic cells.

211 To investigate this further, we performed RT-qPCR analysis of the negative cell cycle regulators,
212 *cdkn1a* and *cdkn2a/b* in the presence and absence of Tp53. We found that *cdkn1a* and *cdkn2a/*b,
213 encoding p21 and p16, respectively, were upregulated in *ahctf1*$^{+/-}$;*tp53*$^{+/+}$;*TO(kras*^{G12V}*)*$^{T/+}$ livers
214 compared to *ahctf1*$^{+/+}$;*tp53*$^{+/+}$;*TO(kras*^{G12V}*)*$^{T/+}$ livers (Fig. 4d). For *cdkn1a*, this response to *ahctf1*
215 heterozygosity was partially dependent on intact Tp53 function. However, while the level of
216 *cdkn2a/b* mRNA expression was increased in response to *ahctf1* heterozygosity in
217 *tp53*$^{+/+}$;*TO(kras*^{G12V}*)*$^{T/+}$ livers, in this case there was no response to *ahctf1* heterozygosity in
218 *tp53*$^{m/m}$;*TO(kras*^{G12V}*)*$^{T/+}$ livers. This is consistent with *cdkn2a/b* expression being regulated solely by
219 Tp53. To understand the basis for the beneficial effects on tumour burden by *ahctf1* heterozygosity
220 in the absence of Tp53, we investigated the impact of *ahctf1* heterozygosity on the expression of
221 *tp53* family members, *tp63* and *tp73*. We found that *tp63* and *tp73* mRNA expression was up-
222 regulated by 3.0-fold and 2.3-fold, respectively in *ahctf1*$^{+/-}$;*tp53*$^{+/+}$;*TO(kras*^{G12V}*)*$^{T/+}$ livers, compared to
223 *ahctf1*$^{+/+}$;*tp53*$^{+/+}$;*TO(kras*^{G12V}*)*$^{T/+}$ livers. Interestingly, the expression of *tp63* and *tp73* was upregulated
224 by almost the same amount in *ahctf1*$^{+/+}$;*tp53*$^{m/m}$;*TO(kras*^{G12V}*)*$^{T/+}$ livers and this was further enhanced
225 by *ahctf1* heterozygosity (Fig. 4e). These data suggest that in response to *ahctf1* heterozygosity,
226 Tp63 and Tp73, like Tp53, may be capable of promoting *cdkn1a* expression to induce cell cycle arrest
227 even in the absence of functional Tp53. Taken together, the data shown in Figs. 3 and 4 show that
228 *ahctf1* heterozygosity constrains *kras*^{G12V}-driven hepatocyte hyperplasia and liver enlargement by a

229 mechanism that results in activation of Tp53 family proteins and initiation of transcriptional
230 programs that induce cell cycle arrest and cell death.

231 ***ahctf1* heterozygosity disrupts the abundance of nuclear pore complexes in *TO(kras^{G12V})$^{T/+}$***
232 **hepatocytes.**

233 To determine how *ahctf1* heterozygosity leads to Tp53 activation, we examined the integrity of
234 some of the essential processes in which the Elys protein plays a role. As depicted in Fig. 1, Elys fulfils
235 many distinct functions during the cell cycle. Starting with post-mitotic nuclear pore assembly (Fig.
236 1a), we used confocal laser-scanning microscopy with Airyscan to look at the abundance and
237 distribution of NPCs in thick sections of liver (200 μm) stained with an antibody (mAb414) that
238 recognises FG-repeat Nups (Nup358, 214, 153 and 62) in mature NPCs. Non-*kras^{G12V}* expressing
239 hepatocytes exhibited fluorescent puncta corresponding to NPCs at the nuclear rim with negligible
240 staining in the cytoplasm, a pattern that was unaffected by *ahctf1* genotype (Fig. 5a; left two
241 columns). Upon induction of expression of the *TO(kras^{G12V})$^{T/+}$* transgene, fluorescence intensity was
242 markedly increased in the presence of wildtype *ahctf1* (Fig 5a, third column) and there was an
243 increase in the ratio of nuclear:cytoplasmic staining (Fig 5b). This pattern was different in
244 hepatocytes on a heterozygous *ahctf1* background. Notably, fluorescence intensity at the nuclear
245 rim was partially diminished and this was concomitant with the appearance of puncta in the
246 cytoplasm (Fig. 5a, fourth column; arrows). This apparent reduction in proper NPC assembly resulted
247 in a 21% reduction in the ratio of nuclear:cytoplasmic fluorescence intensity in liver sections (Fig.
248 5b).

249 To determine the abundance of NPCs, we analysed images acquired at the nuclear surface (Fig. 5c).
250 The pattern and density of fluorescent puncta observed at the nuclear surface of non-*kras^{G12V}*
251 expressing hepatocytes was not affected by *ahctf1* genotype (Fig. 5c; left two columns). We found
252 59% more fluorescent puncta/NPCs at the nuclear surface of hyperplastic hepatocytes expressing
253 *kras^{G12V}* in the presence of wildtype *ahctf1*. This *kras^{G12V}*-driven increase in NPCs was reduced by 20%

254 in response to *ahctf1* heterozygosity (Fig. 5c, d; right two columns). We also observed that induced
255 *kras*^{G12V} expression produced a 28% increase in nuclear volume compared to non-*kras*^{G12V} expressing
256 cells (Fig. 5e), which was reduced to a 13% increase in the context of *ahctf1* heterozygosity.
257 Together, these data indicate that hyperplastic hepatocytes expressing the *kras*^{G12V} oncogene
258 contain more abundant nuclear pores and larger nuclei than their non-*kras*^{G12V} expressing
259 counterparts. While these properties will facilitate nucleocytoplasmic trafficking and be of great
260 benefit towards meeting the transcriptional and translational needs of rapidly cycling cancerous
261 cells, we found that they could not be fully sustained on a *ahctf1*$^{+/-}$ background.

262 ***ahctf1* heterozygosity impairs mitotic spindle assembly and chromosome segregation in**
263 ***TO(kras*^{G12V}*)*$^{T/+}$ hepatocytes**

264 Next, we examined the impact of reduced Elys expression on spindle formation and chromosome
265 segregation (Fig. 1b). We assessed these features in cryosections of liver using α-tubulin and DAPI to
266 stain microtubules and chromatin, respectively. Metaphase cells in *ahctf1*$^{+/+}$*;TO(kras*^{G12V}*)*$^{T/+}$ livers
267 exhibited normal bipolar spindle formation followed by complete chromosome segregation during
268 anaphase (Fig. 6a). In contrast, metaphase cells in *ahctf1*$^{+/-}$*;TO(kras*^{G12V}*)*$^{T/+}$ hepatocytes displayed
269 abnormal multipolar spindles and misaligned chromosomes (Fig. 6b). Proper chromosome
270 segregation was disrupted with multiple anaphase bridges formed. While the distribution of cells
271 observed at different mitotic stages was similar in *ahctf1*$^{+/+}$ and *ahctf1*$^{+/-}$ hepatocytes (Fig. 6c),
272 mitotic abnormalities were observed in 50% of *ahctf1*$^{+/-}$*;TO(kras*^{G12V}*)*$^{T/+}$ hepatocytes during
273 metaphase and anaphase but not at all in *ahctf1*$^{+/+}$*;TO(kras*^{G12V}*)*$^{T/+}$ hepatocytes (Fig. 6d). Taken
274 together, these data suggest that hyperplastic hepatocytes require a full complement of *ahctf1*
275 expression to maintain proper cell division.

276 ***ahctf1* heterozygosity causes DNA damage in *TO(kras*^{G12V}*)*$^{T/+}$ hepatocytes**

277 So far, our results demonstrate that a 50% decrease in *ahctf1* expression has multiple impacts in
278 *TO(kras*^{G12V}*)*$^{T/+}$ hepatocytes, including disrupted NPC assembly, impaired mitotic spindle assembly

279 and incomplete chromosome segregation, consistent with oncogene-induced stress. As several of
280 these defects can converge to produce DNA damage, we looked for evidence of DNA damage by
281 staining cryosections of liver with DAPI and γ-H2AX to mark DNA double-stranded breaks (Fig. 7a,b).
282 We found that while only 1% of *ahctf1*$^{+/+}$*;TO(kras*^{G12V}*)*$^{T/+}$ hepatocyte nuclei were positive for γ-H2AX
283 (Fig. 7c), 6% of *ahctf1*$^{+/+}$*;TO(kras*^{G12V}*)*$^{T/+}$ hepatocyte nuclei were γ-H2AX-positive. Collectively, these
284 data show that the proper functioning of diverse cellular processes in hyperplastic hepatocytes
285 depends on wildtype levels of *ahctf1* expression. We conclude from this that insufficient Elys protein
286 in rapidly cycling cells produces multiple disruptive events that combine to produce elevated levels
287 of oncogene-induced stress and DNA damage, in so doing providing the stimulus to activate Tp53
288 and transcriptional programs that trigger cell cycle arrest and apoptosis.

289 **Combinatorial approaches can completely restrict *kras*^{G12V}-driven liver hyperplasia**

290 Having determined that heterozygous *ahctf1* mutation is effective in restricting *kras*^{G12V}-driven
291 hepatocyte hyperplasia and liver enlargement, we investigated the potential of targeting cancer via
292 another nucleoporin, Ranbp2, in our zebrafish model of HCC. RANBP2 (also known as NUP358) is a
293 major component of the cytoplasmic filaments of NPCs, where it functions in numerous transport
294 pathways. Like ELYS, RANBP2 also plays non-canonical roles outside of the NPC, including in mitotic
295 progression and the maintenance of genome integrity[28-30]. In colon cancer cells with an activated
296 BRAF signature, RANBP2 silencing reduces microtubule outgrowth from kinetochores, inducing
297 spindle perturbations and cell death, the frequency of which can be exacerbated by treatment with
298 microtubule inhibitors[31].

299 We identified our zebrafish *ranbp2* mutant in a transgene assisted ENU-mutagenesis screen for
300 mutations affecting endodermal organ morphogenesis[32] and showed, using whole genome
301 sequencing and homozygosity mapping[33,34], that the underlying mutation was a nonsense mutation
302 in *ranbp2* (Supplementary Fig. 5). Like several other mutants we identified in this screen[8,35,36],

303 mutant *ranbp2* larvae exhibit morphological deficiencies in proliferative compartments, including
304 the developing intestinal epithelium, craniofacial complex and eye (Supplementary Fig. 5).

305 We found that *ranbp2* heterozygosity alone or in combination with *ahctf1* heterozygosity did not
306 impact on liver volume in *2-CLiP* larvae (Fig. 8a,b). In *TO(kras^{G12V})$^{T/+}$* larvae, liver volume was
307 increased 3.8-fold, as observed previously, and the excess liver volume was reduced by 38% and 13%
308 by the introduction of a single mutation in *ahctf1* or *ranbp2*, respectively (Fig. 8b). Remarkably, we
309 found a striking synergistic benefit of trans heterozygosity in *ranbp2$^{+/-}$;ahctf1$^{+/-}$;TO(kras^{G12V})$^{T/+}$*
310 larvae, to the extent that liver volume was no longer distinguishable from that of normal *2-CLiP*
311 livers. These results show that cancer cells are highly susceptible to combinatorial targeting of Nup
312 function and that it may be possible to exploit this vulnerability to produce highly beneficial
313 outcomes without impacting negatively on healthy tissues.

314 To examine this concept in a therapeutic context, we assessed the effect of Selinexor, a selective
315 inhibitor of nuclear export (SINE) in our *kras^{G12V}*-driven liver hyperplasia model. Selinexor is an XPO1
316 (exportin) inhibitor with FDA approval for the treatment of refractory or relapsed multiple myeloma
317 and diffuse large B-cell lymphoma and is in clinical trials for several other cancers, including HCC[37,38].
318 While we observed no reduction in liver volume in *2-CLiP* larvae exposed to 0.10-2.00 µM Selinexor
319 from 5 to 7 dpf (Fig. 8c,d) (Supplementary Fig. 6), *ahctf1$^{+/+}$;TO(kras^{G12V})$^{T/+}$* larvae exhibited a dose-
320 dependent reduction in liver volume when exposed to Selinexor. Strikingly, liver volume was
321 reduced even further in the context of *ahctf1* heterozygosity, such that at a 1.00 µM dose of
322 Selinexor, *kras^{G12V}*-driven hepatocyte hyperplasia was completely blocked and liver volume was
323 indistinguishable from that of normal, non-hyperplastic *2-CLiP* larvae (Fig. 8c,d). These results
324 indicate that XPO1 inhibition is an effective suppressor of growth and proliferation in our model of
325 mutant Kras-driven HCC, and that its effect is even more impressive when combined with a mild
326 reduction in the expression of the nucleoporin, Elys.

327 We next examined whether there was any clinical rationale for developing Nup inhibitors for the
328 purpose of cancer treatment. We analysed the survival data of HCC patients (Fig. 8e) collated in the
329 cBioPortal for Cancer Genomics[39,40] in the context of Nup gene expression (Supplementary Table 3).
330 Median overall survival of patients with high mRNA expression of components of the NUP107-160
331 complex, including ELYS is 21.70 months, whereas the survival of patients with low expression of
332 mRNAs encoding NUP107-160 components is markedly extended to 81.73 months. To be confident
333 of the integrity of this striking result, we investigated whether the gene expression values in the
334 TCGA liver hepatocellular carcinoma (LIHC) dataset were subject to batch effects and unwanted
335 variation, noting that the 372 samples in the LIHC dataset were profiled across 19 sequencing plates.
336 To do this, we performed ANOVAs to assess the effects of individual sequencing plates on the
337 expression of genes encoding components of the NUP107-160 complex (Supplementary Fig. 7).
338 These analyses revealed that differences in gene expression observed between samples were largely
339 unaffected by unwanted variation between sequencing plates.
340

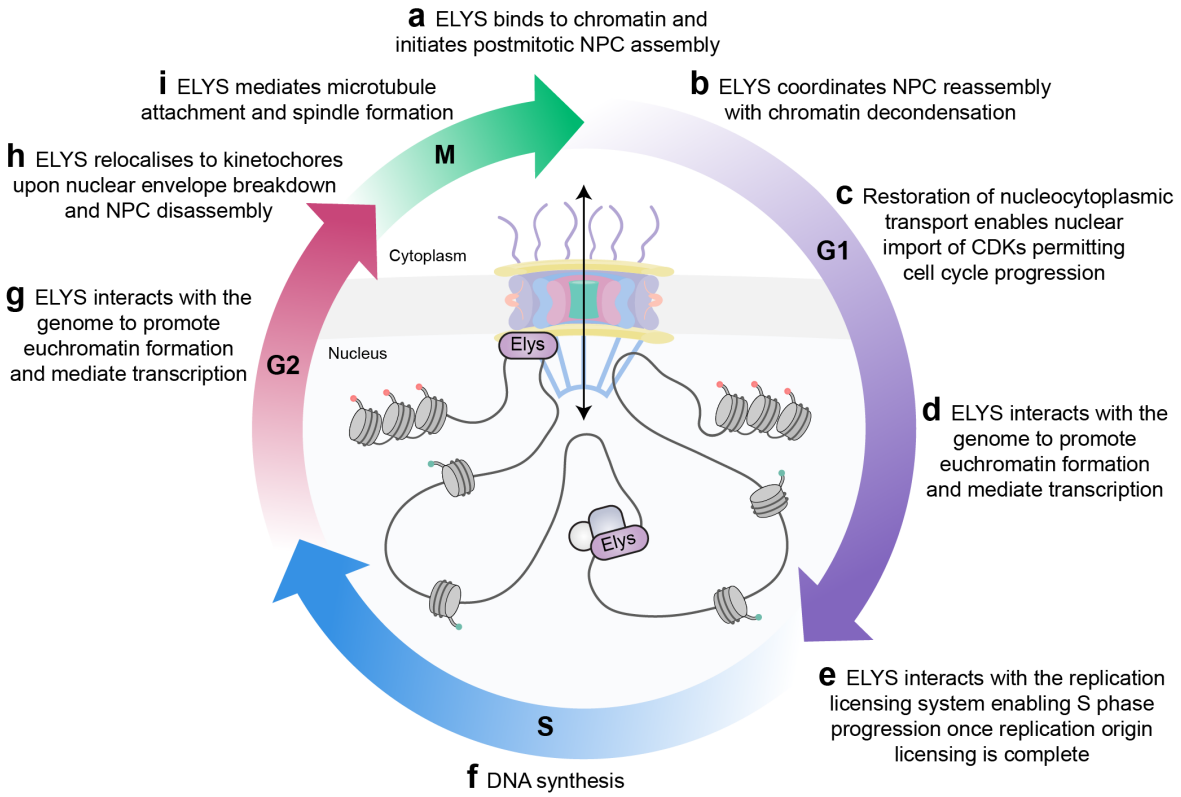

Fig. 1 Elys plays critical roles at several stages of the cell cycle.

Elys is a central player in multiple diverse cellular processes far beyond its canonical role in **a, b.** nuclear pore re-assembly at the end of mitosis. **c.** Elys also restores nucleocytoplasmic trafficking allowing import of cyclin-dependent kinases (CDKs) required for cell cycle progression. **d.** Elys plays an active role in genome regulation through its direct interactions with components of large molecular machineries including chromatin remodellers such as PBAP that favour transcription and **e, f.** the MCM2-7 components of the DNA replication origin licensing system. **g.** After cell growth in G2, **h.** the nuclear envelope breaks down and NPCs are disassembled upon entry into mitosis. Elys relocalises to kinetochores where **i.** it contributes to microtubule attachment and spindle formation.

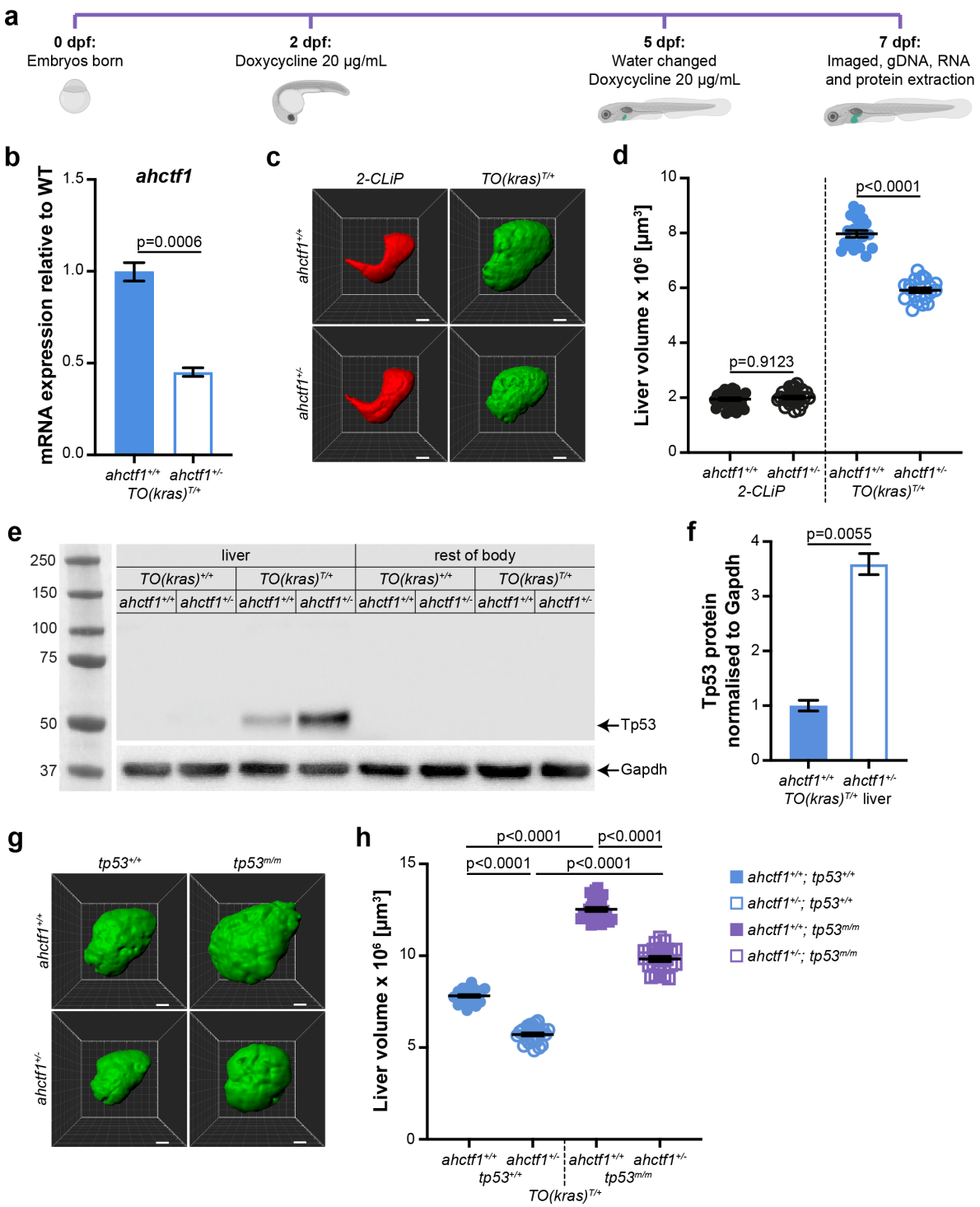

Fig. 2 *ahctf1* heterozygosity reduces liver volume in a zebrafish *kras*^{G12V}-driven model of hepatocellular carcinoma in both Tp53 proficient and deficient larvae.

a. Protocol for doxycycline induction of *TO(kras*^{G12V}*)*$^{T/+}$ expression in developing zebrafish larvae. **b.** RT-qPCR analysis of *ahctf1* mRNA levels in pooled micro-dissected livers (n=3 biological replicates). **c.** Representative three-dimensional reconstructions of *2-CLiP* and *TO(kras*^{G12V}*)*$^{T/+}$ livers of the indicated

358 *ahctf1* genotype. Scale bar 25 µm. **d.** Impact of *ahctf1* heterozygosity on liver volume in *2-CLiP* and

359 *TO(kras^{G12V})$^{T/+}$* larvae (n≥20). **e.** Representative western blot of Tp53 protein signals in lysates of

360 *TO(kras^{G12V})$^{T/+}$* larvae of the indicated *ahctf1* genotype. **f.** Quantification of Tp53 protein levels

361 normalised by reference to the Gapdh loading control (n=3 independent experiments). **g.**

362 Representative three-dimensional reconstructions of *TO(kras^{G12V})$^{T/+}$* livers of the indicated *ahctf1* and

363 *tp53* genotypes. Scale bar 25 µm. **h.** Impact of *ahctf1* heterozygosity and homozygous *tp53* mutation

364 on liver volume in *2-CLiP* and *TO(kras^{G12V})$^{T/+}$* larvae (n≥20). Data are expressed as mean ± SEM.

365 Significance was calculated using a Student's t-test or one-way ANOVA with Tukey's multiple

366 comparisons test.

367

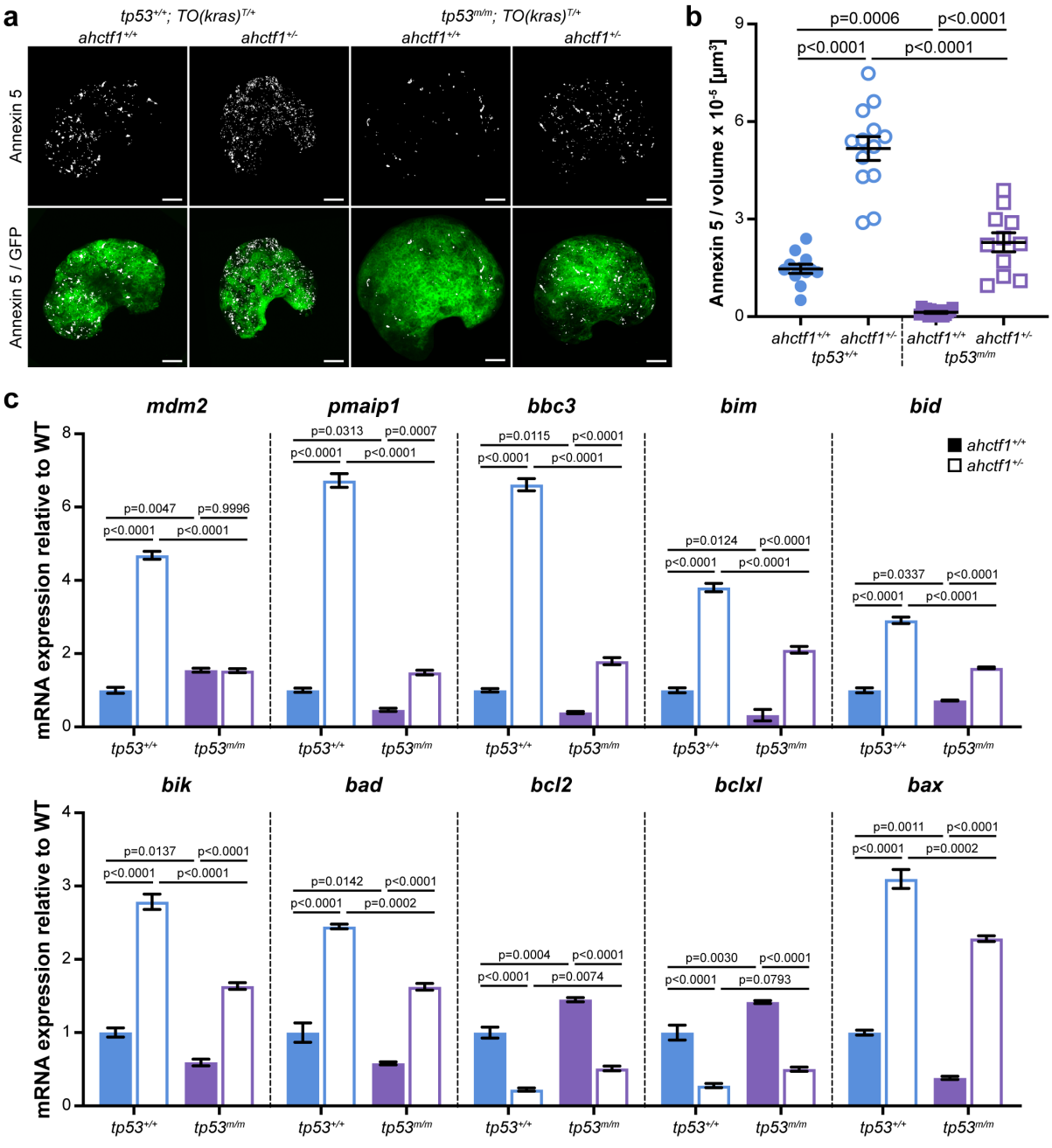

Fig. 3 *ahctf1* heterozygosity increases cell death in *TO(kras^{G12V})$^{T/+}$* hepatocytes in both Tp53 proficient and deficient larvae.

a. Representative maximum intensity projection images of Annexin 5-mKate fluorescence (white puncta), indicating cells undergoing apoptosis in *TO(kras^{G12V})$^{T/+}$* livers of the indicated *ahctf1* and *tp53* genotypes. Scale bar 25 µm. **b.** Quantification of the density of Annexin 5 fluorescent foci in *TO(kras^{G12V})$^{T/+}$* livers of the indicated *ahctf1* and *tp53* genotypes (n≥11). **c.** RT-qPCR analysis of the specified mRNAs in *TO(kras^{G12V})$^{T/+}$* micro-dissected livers of the indicated *ahctf1* and *tp53* genotypes

376 (n=3 biological replicates). Data are expressed as mean ± SEM. Significance was calculated using a

377 one-way ANOVA with Tukey's multiple comparisons test.

378

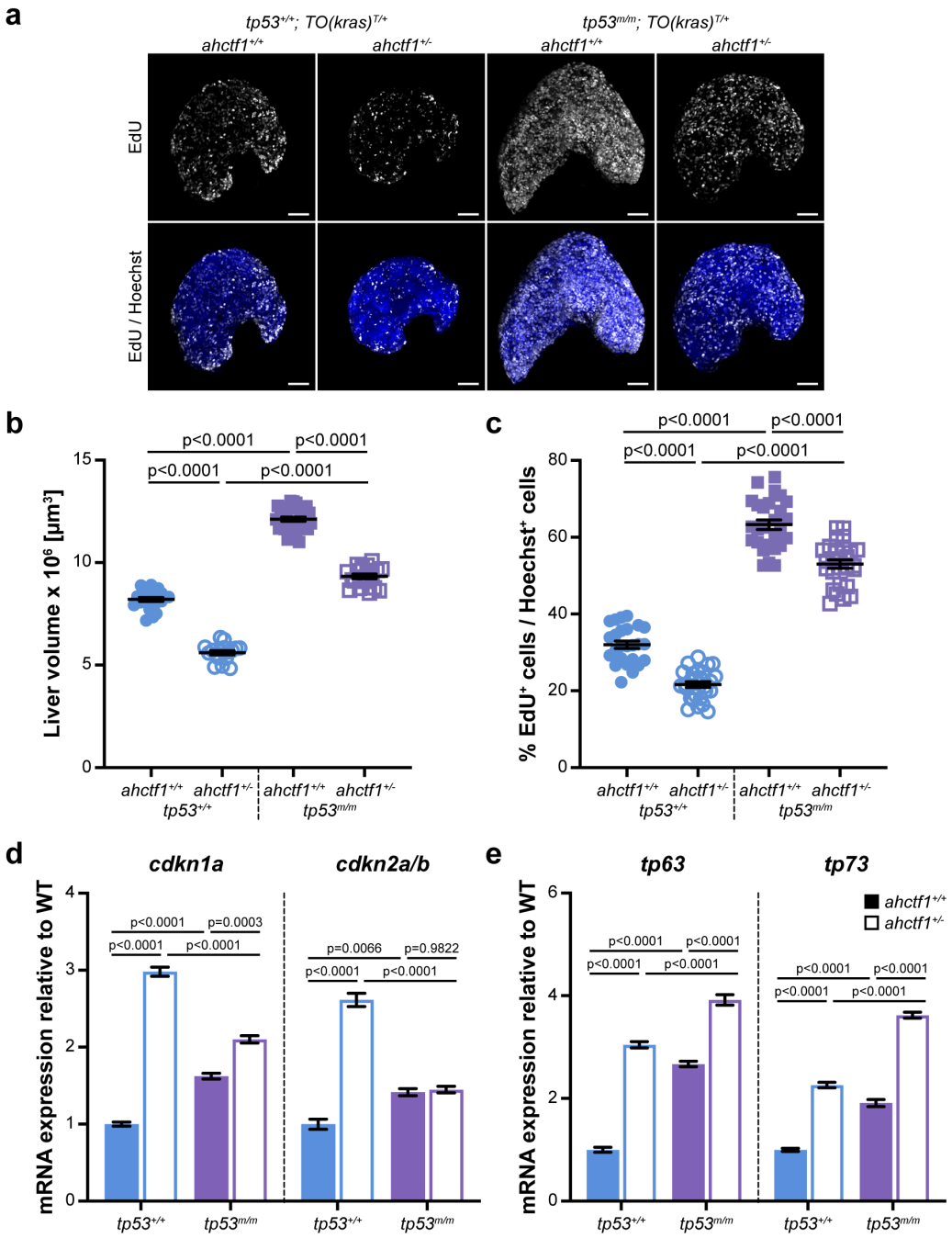

Fig. 4 *ahctf1* heterozygosity restricts DNA replication in *TO(kras^{G12V})$^{T/+}$* hepatocytes.

a. Representative maximum intensity projection images of EdU incorporation (white puncta) into *TO(kras^{G12V})$^{T/+}$* livers of the indicated *ahctf1* and *tp53* genotypes. Scale bar 25 µm. **b.** Impact of *ahctf1* heterozygosity and homozygous *tp53* mutation on liver volume in *2-CLiP* and *TO(kras^{G12V})$^{T/+}$* larvae (n≥17). **c.** Quantification of the percentage of EdU positive nuclei per Hoechst 43332 positive nuclei (n≥25). **d.** RT-qPCR analysis of mRNA expression of the cell cycle regulators, *cdkn1a* and

386 *cdkn2a/b* and **e.** *tp63* and *tp73* in *TO(kras^{G12V})$^{T/+}$* micro-dissected livers of the indicated *ahctf1* and

387 *tp53* genotypes (n=3 biological replicates). Data are expressed as mean ± SEM. Significance was

388 calculated using a one-way ANOVA with Tukey's multiple comparisons test.

389

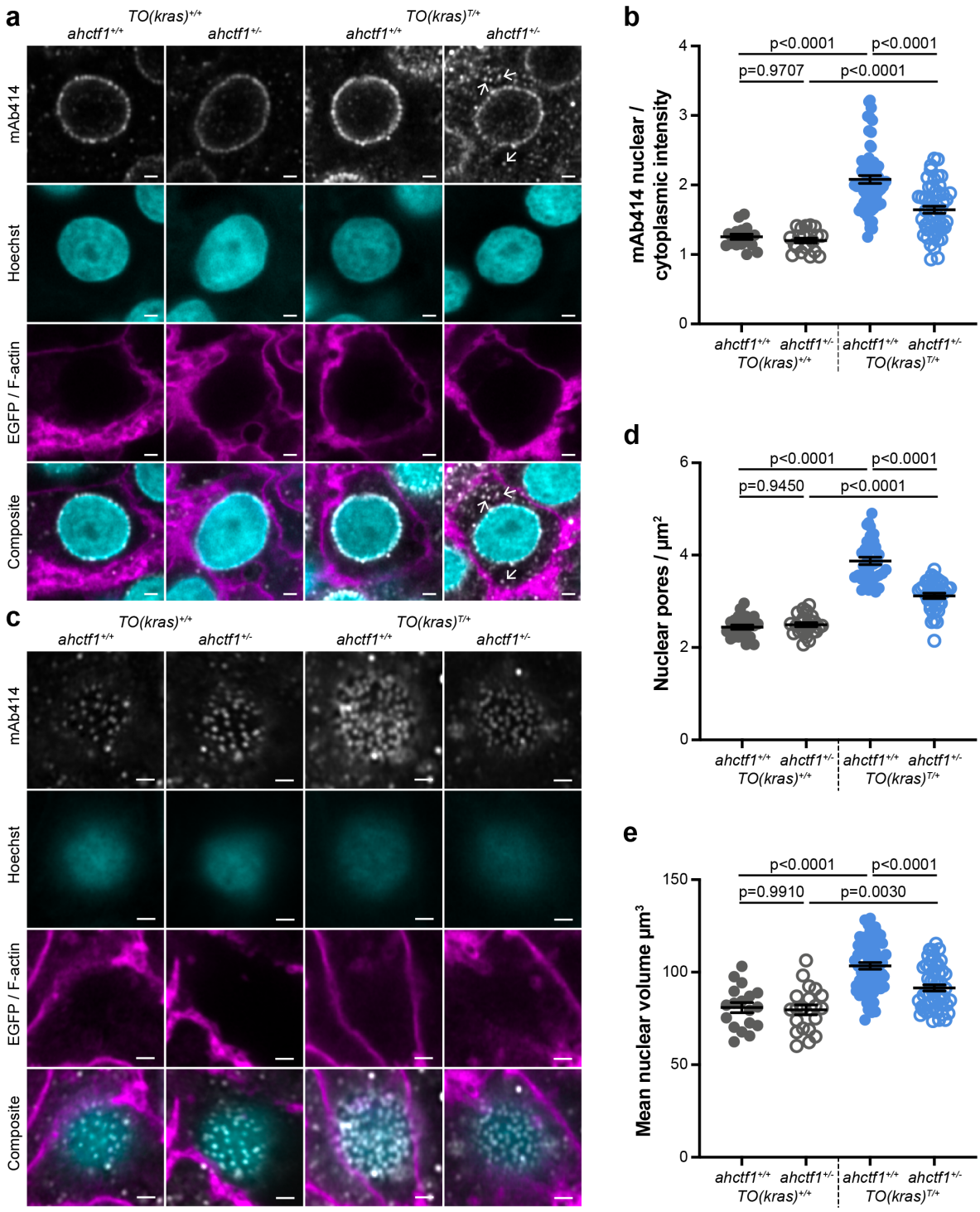

Fig. 5 *ahctf1* heterozygosity disrupts nuclear pore complexes in *TO(kras^{G12V})$^{T/+}$* hepatocytes.

a. Representative Airyscan imaging of liver sections stained with mAb414 (white) marking FG-Nups, Hoechst 43332 (cyan) marking DNA, and rhodamine phalloidin (magenta) marking the F-actin cytoskeleton in non-*TO(kras^{G12V})*-expressing cells or EGFP-Kras^{G12V} (magenta) marking the cell membrane in *TO(kras^{G12V})*-expressing cells of the indicated *ahctf1* and *TO(kras^{G12V})* genotypes.

396 Arrows indicate mAb414/FG-nucleoporin staining in the cytoplasm. Scale bar 2 µm. **b.** Quantification
397 of mean nuclear/cytoplasmic fluorescence intensity of mAb414 staining after 3D segmentation and
398 morphological filtering of nuclear and cytoplasmic areas (n>18). **c.** Representative Airyscan images of
399 mAb414 staining at the nuclear surface of sections of the indicated *ahctf1* and *TO(kras^{G12V})*
400 genotype. Scale bar 1 µm**. d.** Quantification of nuclear pore density (n≥25). **e.** Quantification of
401 nuclear volume (n≥25). Data are expressed as mean ± SEM. Significance was calculated using a one-
402 way ANOVA with Tukey's multiple comparisons test.

403

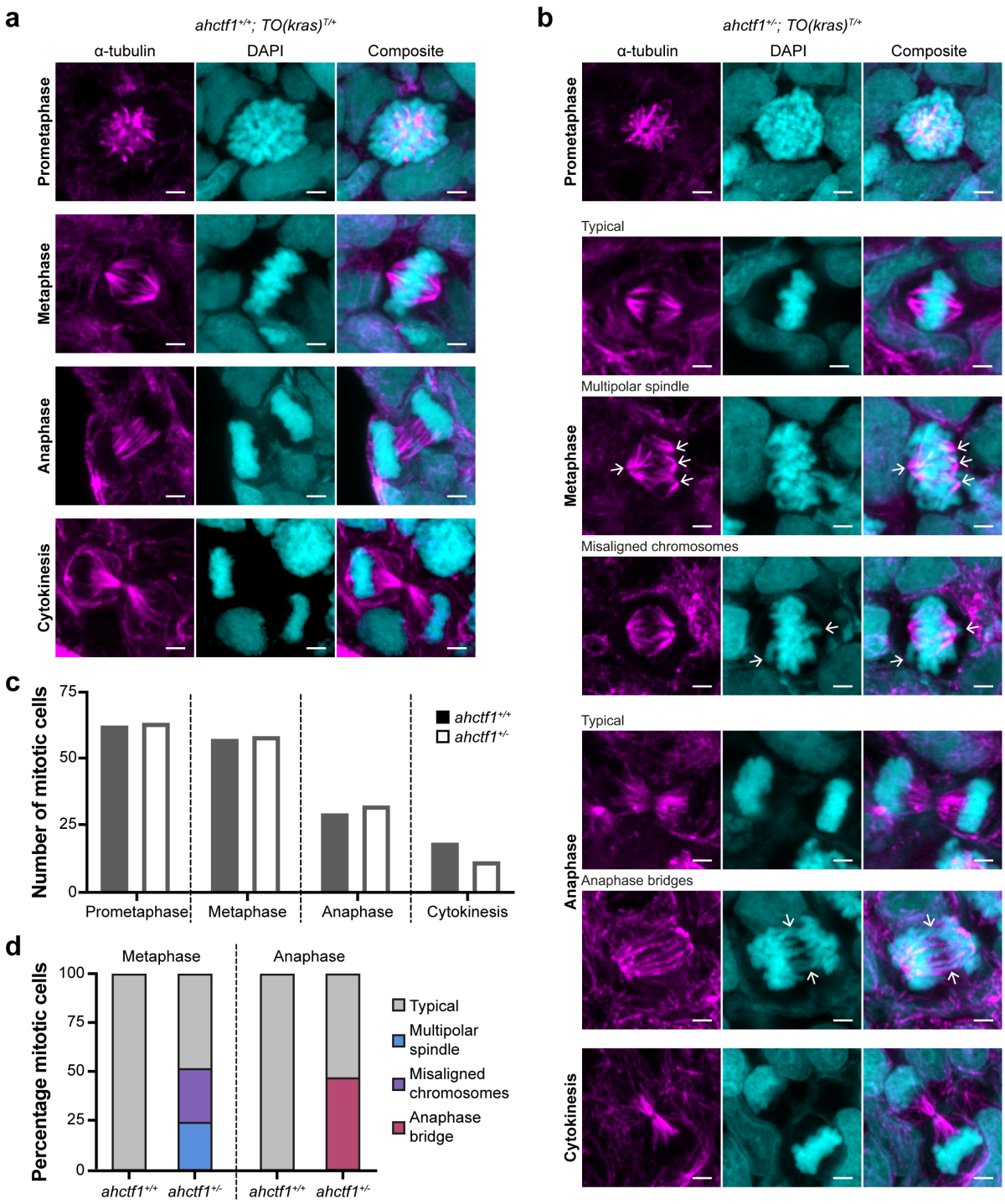

Fig. 6 *ahctf1* heterozygosity impairs mitotic spindle assembly and chromosome segregation in *TO(kras^{G12V})$^{T/+}$* hepatocytes.

a. Representative Airyscan imaging of liver cryosections stained with α-tubulin antibody (magenta) marking spindle microtubules and DAPI (cyan) marking DNA in mitotic cells of *TO(kras^{G12V})$^{T/+}$* larvae on a wildtype *ahctf1$^{+/+}$* background. **b.** Mitotic cells in liver cryosections of *TO(kras^{G12V})$^{T/+}$* larvae on a

410 heterozygous *ahctf1*$^{+/-}$ background exhibit multiple defects, including multipolar spindles, misaligned

411 chromosomes and anaphase bridges (arrows). Scale bar 2 µm. **c.** Distribution of cells observed at

412 different mitotic stages (n=92 livers, 326 mitotic cells) **d.** Quantification of the percentage of mitotic

413 hepatocytes exhibiting an aberrant phenotype (n=14-57).

414

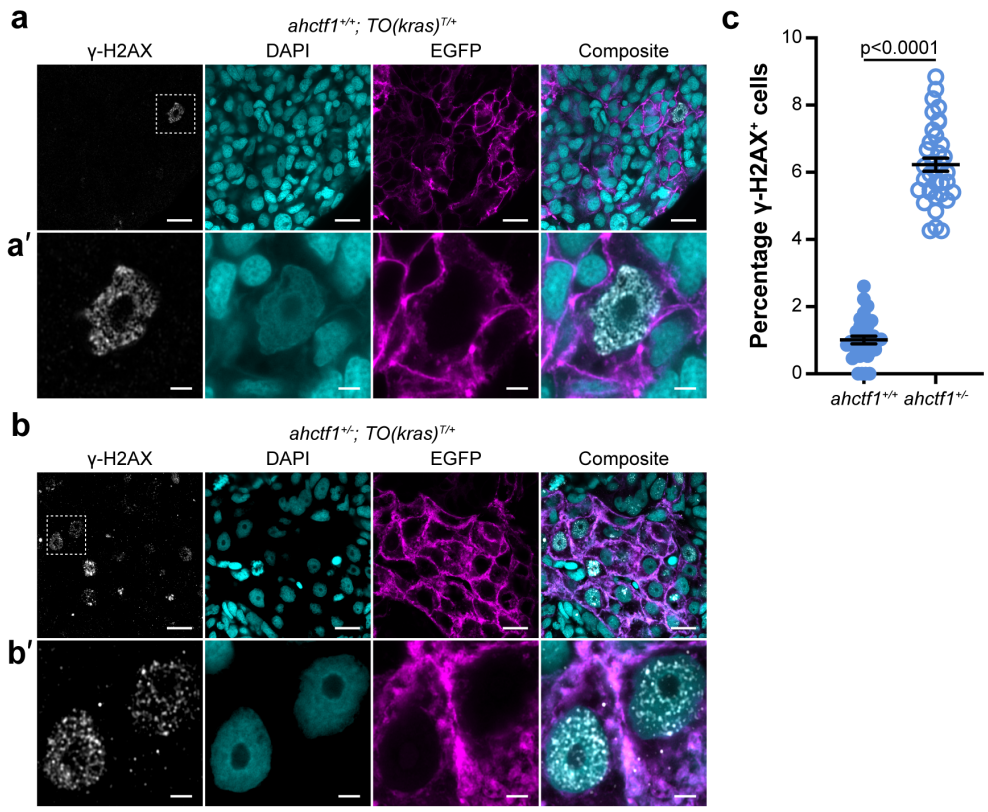

415

416 **Fig. 7 *ahctf1* heterozygosity leads to accumulation of DNA double-strand breaks in *TO(kras^{G12V})$^{T/+}$***

417 **hepatocytes.**

418 **a.** Representative Airyscan imaging of cryosections of liver from *ahctf1$^{+/+}$;TO(kras^{G12V})$^{T/+}$* larvae

419 stained with γ-H2AX antibody (white) marking DNA double-strand breaks, DAPI (cyan) marking DNA

420 and EGFP-Kras^{G12V} (magenta) marking the cell membrane. Scale bar 5 µm. **a'.** Inset of γ-H2AX positive

421 nuclei in *ahctf1$^{+/+}$;TO(kras^{G12V})$^{T/+}$* hepatocytes. Scale bar 2 µm. **b.** Representative images of

422 cryosections of liver from *ahctf1$^{+/-}$;TO(kras^{G12V})$^{T/+}$* larvae. Scale bar 5 µm. **b'.** Inset of γ-H2AX positive

423 nuclei in cryosections of liver from *ahctf1$^{+/-}$;TO(kras^{G12V})$^{T/+}$* larvae. Scale bar 2 µm. **c.** Quantification of

424 the percentage of hepatocytes positive for γ-H2AX (n≥31). Data are expressed as mean ± SEM.

425 Significance was calculated using a Student's t-test.

426

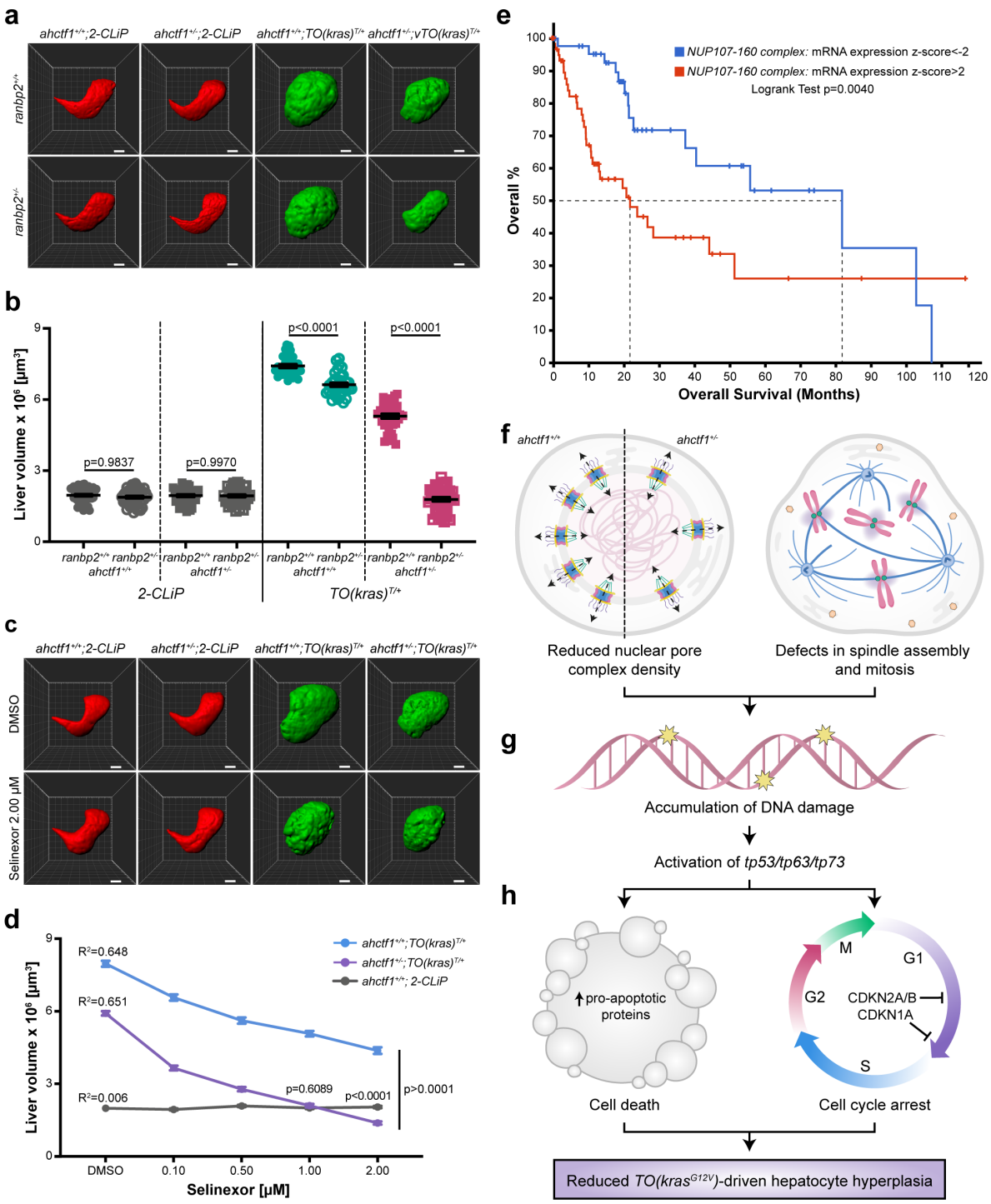

Fig. 8 Combined approaches completely restrict *kras*^{G12V}-driven liver hyperplasia.

a. Representative three-dimensional reconstructions of livers from *2-CLiP* and *TO(kras*^{G12V}*)*$^{T/+}$ larvae of the indicated *ahctf1* and *ranbp2* genotypes. Scale bar 25 µm. **b.** Impact of *ahctf1* heterozygosity and *ranbp2* heterozygosity on liver volume in *2-CLiP* and *TO(kras*^{G12V}*)*$^{T/+}$ larvae (n≥30). Significance was calculated using a one-way ANOVA with Tukey's multiple comparisons test. **c.** Representative

433 three-dimensional reconstructions of *TO(kras^{G12V})$^{T/+}$* livers of the indicated *ahctf1* genotype treated
434 with DMSO or 2.00 µM Selinexor from 5-7 dpf. **d.** Dose-dependent impact of Selinexor treatment
435 (0.10-2.00 µM) on liver volume in *2-CLiP* (grey), *ahctf1$^{+/+}$;TO(kras^{G12V})$^{T/+}$* (blue) and *ahctf1$^{+/-}$*
436 *;TO(kras^{G12V})$^{T/+}$* (purple) larvae (n≥20). Data are expressed as mean ± SEM. Significance was
437 calculated by linear regression analysis. **e.** Overall survival of HCC patients with mRNA expression z-
438 scores >2 for one or more Nup107-160 complex components (red line; 63 cases); median overall
439 survival 21.70 months. Overall survival of HCC patients with mRNA expression z-scores <-2 for one or
440 more Nup107-160 complex components (blue line; 45 cases); median overall survival 81.73 months.
441 Data from the TCGA LIHC dataset (total 372 samples) available in the cBioPortal for Cancer
442 Genomics. **f.** Schematic depiction of two of the processes disrupted by mild depletion of Elys protein
443 culminating in **g.** DNA damage**,** activation of Tp53 transcription programs and **h.** cell death and cell
444 cycle arrest of hyperproliferative Kras^{G12V}-expressing cancer cells.
445

446 **DISCUSSION**

447 In this paper we show that *ahctf1* heterozygosity markedly reduces tumour burden in a genetically
448 engineered zebrafish model of HCC. In this model of mutant *kras*-driven hepatocyte hyperplasia,
449 *ahctf1* heterozygosity produces a reduction in the density of nuclear pores, aberrant chromatid
450 separation during mitosis (Fig. 8f) and accumulation of DNA damage (Fig. 8g). We propose that these
451 events combine to intensify the oncogene-induced stress sensed by cancer cells induced to hyper-
452 proliferate by expression of the $Kras^{G12V}$ oncoprotein. We also show that the heightened levels of
453 oncogene-induced stress caused by mild depletion of Elys protein provide a powerful stimulus to
454 Tp53 activation. We observed increased abundance of Tp53 protein and enhanced transcription of
455 Tp53 target genes, including *pmaip1* and *bbc3*, encoding two pro-apoptotic BH3-only Bcl2 family
456 proteins (aka Noxa and Puma, respectively), and *cdkn1a* and *cdkn2a/b*, encoding the cell cycle arrest
457 proteins, Cdkn1a/p21 and Cdkn2a/b/p16(Ink4a)/p14(Arf) (Fig 8h). Induced expression of these
458 proteins is typically linked to increased apoptosis and cell cycle arrest. We found no evidence that
459 mild depletion of Elys protein activated this sequence of events in unstressed, non-$kras^{G12V}$-
460 expressing cells.

461 Our results suggest that the promising therapeutic effect of inhibiting Elys function could be
462 diminished in cancer cells lacking wild-type Tp53 protein. This is a clinically relevant issue since
463 mutations in *TP53*, or amplification/overexpression of its negative regulators *MDM2*/*MDM4*, occur
464 in 30% of HCC cases[41]. To investigate this further, we conducted experiments on a homozygous *tp53*
465 mutant background. We found that *ahctf1* heterozygosity still produced a 24% reduction in tumour
466 burden and induced cell death in the complete absence of Tp53 function, leading us to consider
467 whether the loss of Tp53 function was compensated for by increased *tp63* and/or *tp73* expression.
468 These genes encode Tp53 family proteins that share considerable structural homology with Tp53,
469 particularly within the DNA binding domain, and can activate common and distinct sets of target
470 genes to produce cell cycle arrest, senescence and apoptosis[42,43]. For example, in response to DNA
471 damage, Tp63 induces senescence and apoptosis in the same way as Tp53, via transcriptional

472 induction of *cdkn1a*, *bbc3* and *pmaip1*[44]. We found that *ahctf1* heterozygosity upregulated *tp63* and
473 *tp73* expression by 3.0-fold and 2.3-fold, respectively, and that this was further enhanced by *tp53*
474 mutation. These results suggest a mechanism through which *ahctf1* heterozygosity achieves a
475 reduction in tumour burden in the absence of Tp53 function. Since *TP63* and *TP73* are rarely
476 mutated in cancer[45], it is plausible that inhibition of ELYS function may still produce a beneficial
477 effect on tumour growth in patients harbouring *TP53* mutations.

478 Dysregulation of nucleocytoplasmic transport is a common feature in a broad spectrum of cancers,
479 usually arising from altered expression of nuclear pore components and/or nuclear transport
480 receptors[46]. For example, overexpression of POM121, a transmembrane NPC component, enhances
481 the nuclear import of the pro-proliferation transcription factors, E2F1, MYC and AR, and increases
482 the therapeutic resistance of prostate cancer[47]. Similarly, the nuclear transport receptor XPO1 is
483 frequently overexpressed in cancers, including HCC, and in this case leads to mis-localisation and
484 inactivation of tumour suppressor proteins[38,48]. As a result, numerous selective inhibitors of nuclear
485 export (SINEs) have been developed, including Selinexor (KPT-330), which has advanced through
486 clinical trials and received FDA approval for the treatment of relapsed or refractory multiple
487 myeloma and diffuse large B-cell lymphoma[37]. We found that Selinexor treatment in our zebrafish
488 HCC model produced a dose-dependent reduction in tumour burden. Moreover, this therapeutic
489 effect was strongly augmented by *ahctf1* heterozygosity, suggesting that new drugs targeting the
490 ELYS protein could be combined effectively with drugs that target nucleocytoplasmic transport. We
491 also exploited the genetic tractability of our zebrafish HCC model to show that trans heterozygosity
492 of *ahctf1*, *ranbp2* delivers a synergistic reduction in liver volume/tumour burden, bringing it back to
493 the volume of non-hyperplastic livers. Notably, non-*TO(kras^{G12V})* livers were completely unaffected
494 by *ahctf1*, *ranbp2* trans heterozygosity, indicating a three-pronged synthetic lethal interaction in
495 cancer cells that may be possible to recapitulate with combinatorial drug treatments.

496 There are several reasons why we think our *TO(kras^{G12V})* zebrafish HCC model provides a clinically
497 relevant *in vivo* platform for the study of human cancer and the discovery of new therapeutic

498 strategies[24]. Firstly, RAS/RAF/MAPK signalling is almost always hyper-activated in human HCC[49].
499 Secondly, the progressive accumulation of histopathologic features including irregular nuclei,
500 cytoplasmic vacuolation and increased vascularisation that are characteristic of tumour progression
501 in HCC are reproduced in the zebrafish model[50]. Thirdly, comparative transcriptomic analysis reveals
502 that the gene expression profile exhibited by oncogenic *kras*^{G12V} hepatocytes isolated from larval
503 zebrafish strongly resembles that of early-stage human HCC, with elevated expression of
504 RAS/RAF/MAPK target genes such as *FGFR4, ETV4, EPHA2, DUSP6* and *SPRY* and DNA damage
505 response genes *GADD45B, CCND1* and *H2AX1*[51].

506 Our results compliment a growing body of evidence that carcinogenesis places persistently high
507 demands on essential cellular genes, including those required for proper nuclear pore function,
508 creating a vulnerability that may be therapeutically targeted without causing adverse effects on
509 normal tissue[52,53]. For example, Sakuma *et al*. used siRNAs targeting 28 out of 32 Nup genes, to
510 reduce the abundance of mature NPCs in the human melanoma-derived cell line, A375[52]. Focusing
511 on two Nups exhibiting a severe reduction in NPC density, this study showed that NUP160 and
512 NUP93 are essential for NPC assembly and that inhibiting this process results in cell death.
513 Moreover, they found that cancer cells exhibited heightened susceptibility to inhibition of NPC
514 assembly compared to human pulmonary fibroblasts and a normal cell line derived from retinal
515 pigmental epithelium (RPE1), which instead underwent reversible cell cycle arrest. The differential
516 sensitivity between cancer cells and normal cells to NPC assembly inhibition is consistent with
517 reports that quiescent cells in normal tissues exist for many years with the same set of assembled
518 NPCs and generally maintain low levels of Nup expression[54,55].

519 The dynamic and diverse functions of ELYS require its binding to Nups and many other proteins,
520 including components of kinetochore and replicative licensing complexes, as well as binding to
521 chromatin in various states of condensation. The molecular topology of the ELYS protein and the
522 structural basis for its diverse protein-protein and protein-chromatin interactions are hitherto poorly
523 defined. Crystal structures of ELYS have shown that the β-propeller and α-helical domains in the N-

524 terminal half of the ELYS protein bind to NUP160, and cryo-electron microscopy reveals the
525 association of the ELYS C-terminal peptide with nucleosomes[21,56]. To advance our molecular
526 understanding of the extent to which discrete domains within the ELYS protein contribute to tumour
527 suppression, further high-resolution structural characterization is required. Hopefully, this will also
528 reveal opportunities to inhibit distinct regions on the protein for the purpose of disabling ELYS
529 function therapeutically. However, even if the topology of ELYS lacked features that would facilitate
530 high affinity binding with small drug-like molecules, as was suggested for other Nups with scaffolding
531 properties[52], rapidly emerging technological advances in drug development are likely to provide
532 alternative strategies to target the ELYS protein. For example, carefully controlled proteasomal
533 degradation of proteins that participate in the oncogenic process with proteolysis targeting chimeras
534 (PROTACs) is a rapidly advancing field in cancer therapy[57]. This approach depends on the availability
535 of a ligand or 'warhead' to direct the PROTAC to the targeted protein, but this need not be a
536 druggable site of protein-protein or protein-chromatin interaction, as is the case for small molecules
537 designed to disrupt the function of the protein. In parallel, emerging small molecule RNA-targeting
538 technology is on course to permit direct modulation of the abundance of specific RNA transcripts for
539 a variety of clinical purposes[58].

540 In summary, we assert that our *in vivo* cancer studies provide a strong and feasible rationale for
541 targeting ELYS for the treatment of a broad spectrum of cancers. Moreover, our observations with
542 RANBP2, indicate that our findings may be extrapolatable to other multi-functional Nups and
543 provide a foundation for effective combinatorial treatments.

544

545 **MATERIALS AND METHODS**

546 **Zebrafish maintenance and strains**

547 Zebrafish were maintained at 28°C on a 12 h light/12 h dark cycle. The mutant lines *ahctf1*^{ti262} and
548 *tp53*$^{M214K/M214K}$ (also known as *tp53*$^{e7/e7}$ and referred to herein as *tp53*$^{m/m}$) have been described
549 previously[7,26]. Tg(*fabp10:dsRed, ela3l:GFP*)^{gz12}, hereafter referred to as *2-CLiP*, expresses dsRed in the
550 liver and GFP in the exocrine pancreas but carries no oncogenic transgenes or mutations[25]. The
551 Tg(*fabp10:rtTA2s-M2;TRE2:EGFP-kras*^{G12V})^{gz32} line referred to as TO(*kras*^{G12V}) and the cell death
552 reporter line, Tg(*actb2:SEC-Hsa.ANXA5-mKate2,cryaa:mCherry*)^{uq24rp} were described previously[24,27].
553 The *ranbp2*^{s452} mutant line was generated in the Liver^{plus} ENU mutagenesis screen[32], and its genetic
554 and morphological characterization is presented in this paper.

555 **Inducing hepatocyte hyperplasia in transgenic zebrafish**

556 To induce mutant *kras*^{G12V} expression, *TO(kras*^{G12V}*)* embryos were treated with 20 µg/mL doxycycline
557 (Sigma, #D9891) at 2 dpf in E3 medium (5 mM NaCl, 0.17 mM KCl, 0.33 mM $CaCl_2$, 0.33 mM $MgSO_4$)
558 with 0.003% 1-Phenyl-2-thiourea (PTU; Sigma, #P7629) to suppress pigmentation. E3 medium was
559 changed at 5 dpf and fresh doxycycline (final conc. 20 µg/mL) added. For the Selinexor experiments,
560 the drug (0.10-2.00 mM) (Karyopharm) or 0.001% DMSO (vehicle control) was added at 5 dpf.
561 Morphological and molecular analyses were performed at 7 dpf. To quantitate liver volume, larvae
562 were anaesthetized with benzocaine (200 mg/L) and mounted in 1% agarose. Image acquisition was
563 performed using an Olympus FVMPE- RS multiphoton microscope with a 25x objective and Olympus
564 FV30-SW software. Excitation wavelengths for GFP and RFP were 840 nm and 1100 nm, respectively.
565 For volumetric analysis of whole livers, z-stacks with step-size 2 µm, were imported into ImageJ or
566 Imaris software.

567

568 **Genotyping**

569 Genomic DNA (gDNA) was extracted from whole zebrafish larvae by incubation at 95°C in 50 µL of 50
570 mM sodium hydroxide (NaOH) for 20 min, followed by neutralization with 5 µL of 1 M Tris-HCl (pH
571 8.0). Primer sequences for genotyping are listed in Supplementary Table 1.

572 **mRNA expression analysis**

573 Total RNA was extracted from independent pools of micro-dissected zebrafish livers using the
574 RNeasy Micro Kit (QIAGEN, #74004). RNA integrity was assessed by a High Sensitivity RNA
575 ScreenTape assay (Agilent, #5067-5579) on a 2200 TapeStation. cDNA was generated from 1-10 µg
576 RNA using the Superscript III First Strand Synthesis System (Invitrogen, #18080051) and oligo(dT)
577 priming according to the manufacturer's instructions. RT-quantitative PCR (RT-qPCR) was performed
578 using a SensiMix SYBR kit (Bioline, #QT605-05) on an Applied Biosystems ViiATM7 Real-Time PCR
579 machine. Expression data were normalized by reference to *hrpt1*, *b2m* and *tbp*. LinRegPCR V11.0
580 was used for baseline correction, PCR efficiency calculation and transcript quantification analysis[59].
581 Relative expression levels were calculated by the $2^{-\Delta\Delta Ct}$ method and all results were expressed as the
582 mean ± SEM of three independent pools of biological replicates. Primer sequences are listed in
583 Supplementary Table 2.

584 **Western blot analysis**

585 Pooled micro-dissected zebrafish livers were lysed in RIPA buffer (20mM Hepes, pH 7.9, 150mM
586 NaCl, 1mM MgCl2, 1% NP40, 10mM NaF, 0.2mM Na3VO4, 10mM β-glycerol phosphate)
587 supplemented with cOmplete Proteinase Inhibitor (Roche, #11836170001) and PhosTOP
588 phosphatase inhibitors (Roche, #04906837001). Samples were incubated for 30 min on ice and the
589 extracts cleared by centrifugation at 13,000 rpm for 20 min at 4°C. The protein concentration of
590 samples was determined by BCA protein assay (Thermo Fisher Scientific, #23227). 25 µg of protein
591 per lane were resolved on NuPAGE Novex Bis-Tris 4-12% polyacrylamide gels (Invitrogen,
592 #NP0321BOX) and transferred onto nitrocellulose blotting membranes (Amersham Protran,

593 #10600003). Membranes were blocked with 5% BSA in PBS for 1 h at RT and incubated with primary
594 antibodies 1:500 Anti-p53 (9.1) mouse mAb (Abcam, #ab77813) overnight at 4°C and 1:1000 Anti-
595 GAPDH (14C10) Rabbit mAb (Cell Signalling Technology, #2118) for 1 h at RT. Secondary antibodies:
596 Goat anti-mouse HRP (Dako, #P0447) and Goat anti-Rabbit HRP (Dako, #P0448), were used at 1:5000
597 and incubated with membranes for 1 h at RT. Signals were developed using Amersham ECL Western
598 Blotting Detection Kit (Cytiva, # RPN2108) and imaged on a Chemidoc Touch (Biorad). Relative
599 protein quantitation was calculated based on normalized integrated intensity.

600 **Cell death analysis**

601 To assess apoptosis, 7 dpf *TO(kras^{G12V});Annexin 5-mKate* zebrafish larvae were fixed in 4%
602 paraformaldehyde (PFA) overnight at 4°C and livers isolated by micro-dissection. Image acquisition
603 was performed using a Zeiss LSM 880 microscope with a 20x objective and ZEN software. Excitation
604 wavelengths for mKate and GFP were 560 nm and 900 nm, respectively. Liver volume was quantified
605 and 3D segmentation of Annexin 5-mKate signals were performed in ImageJ.

606 **Cell cycle analysis**

607 EdU incorporation was used to assess the percentage of cells in S phase of the cell cycle. Briefly, live
608 zebrafish larvae (7 dpf) were incubated at 28°C in 2 mM EdU (Invitrogen, #C10340) in E3 medium for
609 2 h followed by a further incubation in fresh E3 medium for 1 h. Larvae were euthanised using
610 benzocaine (1000 mg/L; Sigma, #PHR1158) prior to removal of the liver by micro-dissection. EdU
611 labelling was carried out using the Click-iT Edu Alexa Fluor 647 (AF647) imaging kit (Invitrogen,
612 #C10340), according to the manufacturer's instructions. The livers were co-stained with Hoechst
613 33342 (Thermofisher, #62249). Image acquisition was performed using an Olympus FVMPE-RS
614 multiphoton microscope with excitation wavelengths of 950 nm for Hoechst 33342 dye and 1160 nm
615 for AF647 (Thermofisher, #A21235). The number of Hoechst 33342 and EdU positive cells was
616 quantified using Arivis Vision4D software.

617 **Nuclear pore analysis**

618 Larvae fixed in 4% PFA overnight at 4°C were embedded in 4% low melting temperature agarose and
619 transverse sections collected at 200 µm intervals using a vibrating microtome (Leica VT 1000S).
620 Sections were blocked with 1% BSA in PBS/0.3% Triton X-100 and incubated with a 1:750 dilution of
621 mAb414 (Abcam, #ab24609) at 4°C overnight. Sections were then incubated with 1:500 anti-mouse
622 AF647 and Hoechst 33342 at room temperature for 1 h. Sections were mounted and imaged using a
623 Zeiss LSM880 Fast Airyscan Confocal microscope with a 63x objective. 3D segmentation of cells was
624 performed in ImageJ using EGFP signal for *TO(kras^{G12V})$^{T/+}$* larvae or F-actin stained with 1:200
625 rhodamine phalloidin for *TO(kras^{G12V})$^{+/+}$* larvae . An outline was drawn around the nuclear periphery
626 as segmented using Hoechst signal. mAb414 fluorescence intensity was calculated for the nuclear
627 periphery and for the cytoplasm. NPC density was calculated by finding maxima for mAb414 at the
628 nuclear surface of 5 nuclei per liver.

629 **Cryosectioning and immunofluorescence microscopy analysis**

630 Dissected livers were fixed in 4% PFA overnight at 4°C and washed with PBS/0.1% Tween 20 before
631 incubation in 30% sucrose in PBS overnight at 4°C. Livers were aligned in a tissue mould, embedded
632 in OCT and frozen on dry ice. The livers were sectioned at 10 µm intervals using a Thermofisher
633 Scientific Microm HM550 cryostat. Sections were washed with PBS before blocking with 10% FCS in
634 PBS/0.3% Triton X-100. Incubation with primary antibodies was performed at 4°C overnight, while
635 incubation with secondary antibodies was performed at room temperature for 1 h. Antibodies used
636 in this work were: 1:2000 α-Tubulin DM1A (CST, #3873), 1:1000 γ-H2AX (gift of James Amatruda),
637 1:250 cleaved caspase 3 (CST, #9664), 1:500 anti-rabbit AF647 (Thermofisher scientific, #A31573)
638 and 1:500 anti-mouse AF647 (Thermofisher, #A21235). Prolong Diamond Antifade reagent with DAPI
639 (Thermofisher #P36962) was used for slide mounting. A Zeiss LSM880 Fast Airyscan Confocal
640 microscope with a 63x objective was used for image acquisition and ImageJ for image analysis.

641 **Statistical analysis**

642 Data are expressed as mean ± SEM unless indicated otherwise and the number of biological
643 replicates indicating samples from individual animals/livers, or pools of individual animals/livers for
644 each experiment are stated in the figure legends. P-values were calculated using Student's *t*-tests
645 (two-tailed, followed by Welch's correction) when comparing two groups, and by ANOVA followed
646 by Tukey's post-hoc test when comparing multiple groups. The effect of Selinexor treatment on liver
647 volume was analysed by linear regression, regressing liver volume against Selinexor concentration.
648 All analysis was performed using GraphPad Prism V7.03 (GraphPad software) and p-values ≤ 0.05
649 were considered statistically significant.

650

651 **ACKNOWLEDGEMENTS**

652 The authors thank Tyson Blanch, Cameron Mackey, Elizabeth Grgacic and Bryan Ko (zebrafish
653 husbandry), Ellen Tsui (histology), James Amatruda (rabbit polyclonal antibody to zebrafish γ-H2AX),
654 Brendon Monahan and Leigh Coultas (insightful discussions).

655 **COMPETING INTERESTS**

656 The authors declare no competing financial interests.

657 **ADDITIONAL INFORMATION**

658 **FUNDING**

659 This work was funded by an Australian Government Research Training Program Scholarship and a
660 WEHI Bridging Fellowship (to KM), the National Health and Medical Research Council of Australia
661 (Grant 1024878 to JKH), Ludwig Cancer Research, a Victorian State Government Operational
662 Infrastructure Support grant, and the Australian Government NHMRC Independent Research
663 Institute Infrastructure Support Scheme.

664 **AUTHORS' CONTRIBUTIONS**

665 KM, KD, JKH conceived and designed the experiments; KM, KD, KS, BH, CS, GB, RM, ATP, TH, EO,
666 DYRS, ZG, JKH developed the methodology; KM, KD, FG, LW, KS, BH, CS, GB, RM, ATP, JKH acquired
667 and analysed the data; KM, KD and JKH wrote the manuscript; KD, JKH supervised the study; JKH
668 acquired the funding.

669 **DATA AVAILABILITY**

670 The datasets generated and/or analysed during the current study are available in the cBioPortal
671 Cancer Genomics database (http://www.cbioportal.org).

672

673 **REFERENCES**

674 1 Gao, S. & Lai, L. Synthetic lethality in drug development: the dawn is coming. *Future Med*
675 *Chem* **10**, 2129-2132, doi:10.4155/fmc-2018-0227 (2018).

676 2 Lord, C. J. & Ashworth, A. PARP inhibitors: Synthetic lethality in the clinic. *Science* **355**, 1152-
677 1158, doi:10.1126/science.aam7344 (2017).

678 3 Luo, J. *et al.* A genome-wide RNAi screen identifies multiple synthetic lethal interactions with
679 the Ras oncogene. *Cell* **137**, 835-848, doi:10.1016/j.cell.2009.05.006 (2009).

680 4 Wang, T. *et al.* Gene Essentiality Profiling Reveals Gene Networks and Synthetic Lethal
681 Interactions with Oncogenic Ras. *Cell* **168**, 890-903 e815, doi:10.1016/j.cell.2017.01.013
682 (2017).

683 5 Solimini, N. L., Luo, J. & Elledge, S. J. Non-oncogene addiction and the stress phenotype of
684 cancer cells. *Cell* **130**, 986-988, doi:10.1016/j.cell.2007.09.007 (2007).

685 6 Okita, K. *et al.* Targeted disruption of the mouse ELYS gene results in embryonic death at
686 peri-implantation development. *Genes Cells* **9**, 1083-1091, doi:10.1111/j.1365-
687 2443.2004.00791.x (2004).

688 7 Chen, J. N. *et al.* Mutations affecting the cardiovascular system and other internal organs in
689 zebrafish. *Development* **123**, 293-302 (1996).

690 8 de Jong-Curtain, T. A. *et al.* Abnormal nuclear pore formation triggers apoptosis in the
691 intestinal epithelium of elys-deficient zebrafish. *Gastroenterology* **136**, 902-911,
692 doi:10.1053/j.gastro.2008.11.012 (2009).

693 9 Davuluri, G. *et al.* Mutation of the zebrafish nucleoporin elys sensitizes tissue progenitors to
694 replication stress. *PLoS Genet* **4**, e1000240, doi:10.1371/journal.pgen.1000240 (2008).

695 10 Rasala, B. A., Orjalo, A. V., Shen, Z., Briggs, S. & Forbes, D. J. ELYS is a dual
696 nucleoporin/kinetochore protein required for nuclear pore assembly and proper cell
697 division. *Proceedings of the National Academy of Sciences of the United States of America*
698 **103**, 17801-17806, doi:10.1073/pnas.0608484103 (2006).

699 11 Gillespie, P. J., Khoudoli, G. A., Stewart, G., Swedlow, J. R. & Blow, J. J. ELYS/MEL-28
700 chromatin association coordinates nuclear pore complex assembly and replication licensing.
701 *Curr Biol* **17**, 1657-1662, doi:10.1016/j.cub.2007.08.041 (2007).
702 12 Franz, C. *et al.* MEL-28/ELYS is required for the recruitment of nucleoporins to chromatin
703 and postmitotic nuclear pore complex assembly. *EMBO reports* **8**, 165-172,
704 doi:10.1038/sj.embor.7400889 (2007).
705 13 Beck, M. & Hurt, E. The nuclear pore complex: understanding its function through structural
706 insight. *Nature reviews. Molecular cell biology* **18**, 73-89, doi:10.1038/nrm.2016.147 (2017).
707 14 Hodgson, B., Li, A., Tada, S. & Blow, J. J. Geminin becomes activated as an inhibitor of
708 Cdt1/RLF-B following nuclear import. *Curr Biol* **12**, 678-683, doi:10.1016/s0960-
709 9822(02)00778-9 (2002).
710 15 Kuhn, T. M., Pascual-Garcia, P., Gozalo, A., Little, S. C. & Capelson, M. Chromatin targeting of
711 nuclear pore proteins induces chromatin decondensation. *J Cell Biol* **218**, 2945-2961,
712 doi:10.1083/jcb.201807139 (2019).
713 16 Guttinger, S., Laurell, E. & Kutay, U. Orchestrating nuclear envelope disassembly and
714 reassembly during mitosis. *Nature reviews. Molecular cell biology* **10**, 178-191,
715 doi:10.1038/nrm2641 (2009).
716 17 Chatel, G. & Fahrenkrog, B. Nucleoporins: leaving the nuclear pore complex for a successful
717 mitosis. *Cell Signal* **23**, 1555-1562, doi:10.1016/j.cellsig.2011.05.023 (2011).
718 18 Mishra, R. K., Chakraborty, P., Arnaoutov, A., Fontoura, B. M. & Dasso, M. The Nup107-160
719 complex and gamma-TuRC regulate microtubule polymerization at kinetochores. *Nat Cell*
720 *Biol* **12**, 164-169, doi:10.1038/ncb2016 (2010).
721 19 Orjalo, A. V. *et al.* The Nup107-160 nucleoporin complex is required for correct bipolar
722 spindle assembly. *Mol Biol Cell* **17**, 3806-3818, doi:10.1091/mbc.e05-11-1061 (2006).

723 20 Yokoyama, H. *et al.* The nucleoporin MEL-28 promotes RanGTP-dependent gamma-tubulin
724 recruitment and microtubule nucleation in mitotic spindle formation. *Nat Commun* **5**, 3270,
725 doi:10.1038/ncomms4270 (2014).
726 21 Kobayashi, W. *et al.* Structural and biochemical analyses of the nuclear pore complex
727 component ELYS identify residues responsible for nucleosome binding. *Commun Biol* **2**, 163,
728 doi:10.1038/s42003-019-0385-7 (2019).
729 22 Bilokapic, S. & Schwartz, T. U. Molecular basis for Nup37 and ELY5/ELYS recruitment to the
730 nuclear pore complex. *Proceedings of the National Academy of Sciences of the United States*
731 *of America* **109**, 15241-15246, doi:10.1073/pnas.1205151109 (2012).
732 23 Rasala, B. A., Ramos, C., Harel, A. & Forbes, D. J. Capture of AT-rich chromatin by ELYS
733 recruits POM121 and NDC1 to initiate nuclear pore assembly. *Mol Biol Cell* **19**, 3982-3996,
734 doi:10.1091/mbc.E08-01-0012 (2008).
735 24 Chew, T. W. *et al.* Crosstalk of Ras and Rho: activation of RhoA abates Kras-induced liver
736 tumorigenesis in transgenic zebrafish models. *Oncogene* **33**, 2717-2727,
737 doi:10.1038/onc.2013.240 (2014).
738 25 Korzh, S. *et al.* Requirement of vasculogenesis and blood circulation in late stages of liver
739 growth in zebrafish. *BMC Dev Biol* **8**, 84, doi:10.1186/1471-213X-8-84 (2008).
740 26 Berghmans, S. *et al.* tp53 mutant zebrafish develop malignant peripheral nerve sheath
741 tumors. *Proceedings of the National Academy of Sciences of the United States of America*
742 **102**, 407-412, doi:10.1073/pnas.0406252102 (2005).
743 27 Hall, T. E. *et al.* Cellular rescue in a zebrafish model of congenital muscular dystrophy type
744 1A. *NPJ Regen Med* **4**, 21, doi:10.1038/s41536-019-0084-5 (2019).
745 28 Joseph, J., Liu, S. T., Jablonski, S. A., Yen, T. J. & Dasso, M. The RanGAP1-RanBP2 complex is
746 essential for microtubule-kinetochore interactions in vivo. *Curr Biol* **14**, 611-617,
747 doi:10.1016/j.cub.2004.03.031 (2004).

748 29 Salina, D., Enarson, P., Rattner, J. B. & Burke, B. Nup358 integrates nuclear envelope
749 breakdown with kinetochore assembly. *J Cell Biol* **162**, 991-1001,
750 doi:10.1083/jcb.200304080 (2003).
751 30 Hashizume, C., Kobayashi, A. & Wong, R. W. Down-modulation of nucleoporin
752 RanBP2/Nup358 impaired chromosomal alignment and induced mitotic catastrophe. *Cell*
753 *Death Dis* **4**, e854, doi:10.1038/cddis.2013.370 (2013).
754 31 Vecchione, L. *et al.* A Vulnerability of a Subset of Colon Cancers with Potential Clinical Utility.
755 *Cell* **165**, 317-330, doi:10.1016/j.cell.2016.02.059 (2016).
756 32 Ober, E. A., Verkade, H., Field, H. A. & Stainier, D. Y. Mesodermal Wnt2b signalling positively
757 regulates liver specification. *Nature* **442**, 688-691, doi:10.1038/nature04888 (2006).
758 33 Leshchiner, I. *et al.* Mutation mapping and identification by whole-genome sequencing.
759 *Genome Res* **22**, 1541-1548, doi:10.1101/gr.135541.111 (2012).
760 34 Voz, M. L. *et al.* Fast homozygosity mapping and identification of a zebrafish ENU-induced
761 mutation by whole-genome sequencing. *PLoS One* **7**, e34671,
762 doi:10.1371/journal.pone.0034671 (2012).
763 35 Boglev, Y. *et al.* Autophagy induction is a Tor- and Tp53-independent cell survival response
764 in a zebrafish model of disrupted ribosome biogenesis. *PLoS Genet* **9**, e1003279,
765 doi:10.1371/journal.pgen.1003279 (2013).
766 36 Markmiller, S. *et al.* Minor class splicing shapes the zebrafish transcriptome during
767 development. *Proceedings of the National Academy of Sciences of the United States of*
768 *America* **111**, 3062-3067, doi:10.1073/pnas.1305536111 (2014).
769 37 Jans, D. A., Martin, A. J. & Wagstaff, K. M. Inhibitors of nuclear transport. *Curr Opin Cell Biol*
770 **58**, 50-60, doi:10.1016/j.ceb.2019.01.001 (2019).
771 38 Zheng, Y. *et al.* KPT-330 inhibitor of XPO1-mediated nuclear export has anti-proliferative
772 activity in hepatocellular carcinoma. *Cancer Chemother Pharmacol* **74**, 487-495,
773 doi:10.1007/s00280-014-2495-8 (2014).

774 39 Cerami, E. *et al.* The cBio cancer genomics portal: an open platform for exploring
775 multidimensional cancer genomics data. *Cancer Discov* **2**, 401-404, doi:10.1158/2159-
776 8290.CD-12-0095 (2012).
777 40 Gao, J. *et al.* Integrative analysis of complex cancer genomics and clinical profiles using the
778 cBioPortal. *Sci Signal* **6**, pl1, doi:10.1126/scisignal.2004088 (2013).
779 41 Zucman-Rossi, J., Villanueva, A., Nault, J. C. & Llovet, J. M. Genetic Landscape and
780 Biomarkers of Hepatocellular Carcinoma. *Gastroenterology* **149**, 1226-1239 e1224,
781 doi:10.1053/j.gastro.2015.05.061 (2015).
782 42 Levrero, M. *et al.* The p53/p63/p73 family of transcription factors: overlapping and distinct
783 functions. *J Cell Sci* **113 (Pt 10)**, 1661-1670 (2000).
784 43 Suh, E. K. *et al.* p63 protects the female germ line during meiotic arrest. *Nature* **444**, 624-
785 628, doi:10.1038/nature05337 (2006).
786 44 Kerr, J. B. *et al.* DNA damage-induced primordial follicle oocyte apoptosis and loss of fertility
787 require TAp63-mediated induction of Puma and Noxa. *Mol Cell* **48**, 343-352,
788 doi:10.1016/j.molcel.2012.08.017 (2012).
789 45 Dotsch, V., Bernassola, F., Coutandin, D., Candi, E. & Melino, G. p63 and p73, the ancestors
790 of p53. *Cold Spring Harb Perspect Biol* **2**, a004887, doi:10.1101/cshperspect.a004887 (2010).
791 46 Kau, T. R., Way, J. C. & Silver, P. A. Nuclear transport and cancer: from mechanism to
792 intervention. *Nat Rev Cancer* **4**, 106-117, doi:10.1038/nrc1274 (2004).
793 47 Rodriguez-Bravo, V. *et al.* Nuclear Pores Promote Lethal Prostate Cancer by Increasing
794 POM121-Driven E2F1, MYC, and AR Nuclear Import. *Cell* **174**, 1200-1215 e1220,
795 doi:10.1016/j.cell.2018.07.015 (2018).
796 48 Hill, R., Cautain, B., de Pedro, N. & Link, W. Targeting nucleocytoplasmic transport in cancer
797 therapy. *Oncotarget* **5**, 11-28, doi:10.18632/oncotarget.1457 (2014).
798 49 Calvisi, D. F. *et al.* Ubiquitous activation of Ras and Jak/Stat pathways in human HCC.
799 *Gastroenterology* **130**, 1117-1128, doi:10.1053/j.gastro.2006.01.006 (2006).

800 50 Zheng, W. *et al.* Xmrk, kras and myc transgenic zebrafish liver cancer models share
801 molecular signatures with subsets of human hepatocellular carcinoma. *PLoS One* **9**, e91179,
802 doi:10.1371/journal.pone.0091179 (2014).
803 51 Huo, X. *et al.* Transcriptomic analyses of oncogenic hepatocytes reveal common and
804 different molecular pathways of hepatocarcinogenesis in different developmental stages
805 and genders in kras(G12V) transgenic zebrafish. *Biochem Biophys Res Commun* **510**, 558-
806 564, doi:10.1016/j.bbrc.2019.02.008 (2019).
807 52 Sakuma, S. *et al.* Inhibition of Nuclear Pore Complex Formation Selectively Induces Cancer
808 Cell Death. *Cancer Discov* **11**, 176-193, doi:10.1158/2159-8290.CD-20-0581 (2021).
809 53 Beck, M., Schirmacher, P. & Singer, S. Alterations of the nuclear transport system in
810 hepatocellular carcinoma - New basis for therapeutic strategies. *J Hepatol* **67**, 1051-1061,
811 doi:10.1016/j.jhep.2017.06.021 (2017).
812 54 D'Angelo, M. A., Raices, M., Panowski, S. H. & Hetzer, M. W. Age-dependent deterioration of
813 nuclear pore complexes causes a loss of nuclear integrity in postmitotic cells. *Cell* **136**, 284-
814 295, doi:10.1016/j.cell.2008.11.037 (2009).
815 55 Toyama, B. H. *et al.* Identification of long-lived proteins reveals exceptional stability of
816 essential cellular structures. *Cell* **154**, 971-982, doi:10.1016/j.cell.2013.07.037 (2013).
817 56 Bilokapic, S. & Schwartz, T. U. Structural and functional studies of the 252 kDa nucleoporin
818 ELYS reveal distinct roles for its three tethered domains. *Structure* **21**, 572-580,
819 doi:10.1016/j.str.2013.02.006 (2013).
820 57 Ocana, A. & Pandiella, A. Proteolysis targeting chimeras (PROTACs) in cancer therapy. *J Exp*
821 *Clin Cancer Res* **39**, 189, doi:10.1186/s13046-020-01672-1 (2020).
822 58 Mukherjee, H. *et al.* PEARL-seq: A Photoaffinity Platform for the Analysis of Small Molecule-
823 RNA Interactions. *ACS Chem Biol* **15**, 2374-2381, doi:10.1021/acschembio.0c00357 (2020).
824 59 Ruijter, J. M. *et al.* Amplification efficiency: linking baseline and bias in the analysis of
825 quantitative PCR data. *Nucleic Acids Res* **37**, e45, doi:10.1093/nar/gkp045 (2009).